

## Achieving a 2.7 V aqueous hybrid supercapacitor by the pH-regulation of electrolyte

Lijun Su,<sup>a,b</sup> Qingnuan Zhang,<sup>a</sup> Yue Wang,<sup>c</sup> Jianing Meng,<sup>c</sup> Yongtai Xu,<sup>a,b</sup> Lingyang Liu,<sup>a,b</sup> and Xingbin Yan<sup>\*a,b,d</sup>

<sup>a</sup> Laboratory of Clean Energy Chemistry and Materials, State Key Laboratory of Solid Lubrication, Lanzhou Institute of Chemical Physics, Chinese Academy of Sciences, Lanzhou 730000, P.R. China.

<sup>b</sup> Center of Materials Science and Optoelectronics Engineering, University of Chinese Academy of Sciences, Beijing 100049, P.R. China.

<sup>c</sup> School of Physical Science and Technology, Lanzhou University, Lanzhou, 730000, P.R. China.

<sup>d</sup> Dalian National Laboratory for Clean Energy, Dalian 116023, P.R. China.

\*Corresponding author: XingBin Yan (email: xbyan@licp.cas.cn)

**Keywords:** hybrid supercapacitor, aqueous electrolyte, pH regulation, voltage window

**Abstract:** The output voltage directly determines the energy density of supercapacitors (SCs), and it is closely associated with the types of electrolytes. Here we demonstrate the great feasibility of using a pH-regulation strategy in neutral sodium sulfate electrolyte to widen the voltage window (0-1.3 V) and to achieve an additional redox capacity (234% increase) for sodium-embedded manganese

oxide/nitrogen-doped graphene (denoted as NMO-NDs@NG) electrode at the same time. The mechanism of strategy was systematically explored by using various in-situ and ex-situ characterizations as well as density function theory calculations. The NMO-NDs@NG showed a surface-controlled pseudocapacitive behavior in the neutral electrolyte, but mainly displayed a battery-like behavior in the alkaline electrolyte. Properly increasing the pH value of the initial neutral electrolyte, the emerging reversible redox reaction effectively inhibited the water decomposition occurred on the electrode surface, thereby expanding the voltage window as well as increasing the capacity. Based on this, an aqueous hybrid SC was assembled, which was able to work at 2.7 V, and presented a maximum energy density of 68 Wh kg<sup>-1</sup> and a maximum power density of 27 kW kg<sup>-1</sup>. The results presented here provide a useful strategy for achieving high-voltage and high-capacity aqueous SCs.

## Introduction

Aqueous supercapacitors (SCs) have been received great research interest because they not only hold the outstanding power output performance of SCs, but also have advantages with respect to low-cost, high-level safety and low environmental impact.<sup>1-9</sup> However, the key challenge for aqueous SCs is their narrow voltage window that generally result in low energy density, thereby it is difficult to meet the demand of long-endurance electronic devices.<sup>10-12</sup> The increase of voltage window unduly will lead to the decomposition of water near the electrode surface, resulting in poor period life of SCs.<sup>13-15</sup> Therefore, to figure out this issue, expanding

electrochemical stability window (ESW) of aqueous electrolytes is of top priority for developing high-performance aqueous SCs.<sup>10, 16, 17</sup> Up to now, some modification strategies have been explored to extend the ESW of aqueous SCs, and they can be mainly divided into two orientations. **One** is from the perspective of electrode materials: balancing the mass between two electrodes,<sup>18-22</sup> passivating the surface of electrode,<sup>23, 24</sup> **modifying the potential of zero charge (pzc) of electrode**,<sup>25-27</sup> using iron-based materials with wide negative **voltage window** in neutral or alkaline electrolytes as negative electrodes,<sup>28</sup> using cation-intercalated manganese oxides with wide positive **voltage window** in neutral electrolytes as positive electrodes,<sup>29, 30</sup> and so on. Among these reports, the largest **voltage window** of 2.7 V was achieved by Xiong *et al.*, where they fabricated an asymmetric supercapacitor (ASC) by employing Na<sub>0.25</sub>MnO<sub>2</sub> nanosheets as cathode and porous carbon as anode.<sup>31</sup> The other is from the modification of electrolytes: introducing redox-active additives in electrolytes,<sup>29, 32, 33</sup> and using highly concentrated “water in salt” (WIS) electrolytes and hydrate-melt electrolytes.<sup>34-37</sup> Among these reports, the largest **voltage window** of 3.0 V was achieved by An *et al.*, where they used an expensive lithium bistrifluoromethanesulfonimide (LiTFSI) WIS electrolyte.<sup>38</sup> Comparatively speaking, the electrolyte-modification strategy is easier to implement and more suitable for the actual industrial manufacturing of SCs.

As we can see from aforementioned modifying strategies, the fundamental purpose of broadening ESW is to suppressing hydrogen evolution reaction (HER) and/or oxygen evolution reaction (OER) of water at the near surface of electrode.<sup>39</sup> However,

as shown in Pourbaix diagram (Figure S1), the overall ESW of aqueous electrolytes remains thermodynamic constant at 1.23 V.<sup>34</sup> According to Nernst Equation, the overpotentials of HER and OER are respectively related to **the hydrogen ions concentration and the hydroxide ions concentration**.<sup>40</sup> There are mainly three kinds of **overpotentials in aqueous SCs**, namely activation overpotential, resistance overpotential and concentration overpotential. Activation overpotential is involved in chemical reactions prior to electron transfer and produce a high enough current **for the redox reaction**.<sup>41</sup> Resistance overpotential associates with electrode surface and interface resistance, including electrolyte diffusion, surface polarization, and so on.<sup>42</sup> Concentration overpotential is generated by the difference of ionic concentration between bulk electrolyte and electrode surface.<sup>43</sup> The activation overpotential and resistance overpotential can dynamically compensate for the limitations of **voltage window** owing to the hydrolysis. Clearly, the overpotential of the electrodes plays a central role in determining the maximum **voltage window** of aqueous SCs. And the magnitude of the overpotential depends on the potential of hydrogen (pH) value.<sup>44, 45</sup> Therefore, through adjusting the pH of the electrolytes to control the overpotential should be a promising strategy to extend the ESW of aqueous SCs.

In this work, a new **positive electrode material**, i.e. sodium-embedded manganese oxide nano-dots loaded on nitrogen-doped graphene (NMO-NDs@NG), is prepared by using a two-step solvothermal method. We adopt a pH-regulation strategy in neutral sodium sulfate electrolyte to widen the **voltage window** and to **achieve additional capacity** at the same time. **The analyses of in-situ Raman, electrochemical**

quartz crystal microbalance (EQCM), in-situ XRD, ex-situ XPS and density function theory (DFT) calculations confirm that, the NMO-NDs@NG chiefly displays a surface-controlled pseudocapacitive behavior in the neutral electrolyte, but it mainly displays a battery-like behavior in the alkaline electrolyte. Properly increasing the pH value is able to widen the overpotential of oxygen evolution and effectively enhance reversible redox reaction of the NMO-NDs@NG electrode. Under pH=9 condition, this electrode exhibits a widening voltage window of 0-1.3 V and the capacity increased to 234% of the initial value in neutral electrolyte. Subsequently, an aqueous hybrid SC is assembled by using an iron-based material (FeOOH) as the negative electrode, the NMO-NDs@NG as the positive electrode and the pH-regulated Na<sub>2</sub>SO<sub>4</sub> solution as the electrolyte. The as-fabricated ASC is able to work at 2.7 V stably, and exhibits a maximum energy density of 68 Wh kg<sup>-1</sup> and a maximum power density of 27 kW kg<sup>-1</sup>. The results fully verify the effectiveness of the pH-regulation of electrolyte to build better aqueous hybrid SCs.

## Experimental Section

### Preparation of NMO-NDs@NG

Firstly, GO powder was synthesized by Hummers method.<sup>46, 47</sup> 20 mg of GO was dispersed in 20 ml of N,N-dimethylformamide (DMF) and sonicated for 6 h. Then, 20 mg of Mn<sub>2</sub>(CO)<sub>10</sub> was dissolved in 10 ml DMF and poured into GO suspension. After that, 0.25 ml of octylamine was added into the above mixed solution and sonicated for 30 min. Finally, the mixture was transferred to a Teflon-lined stainless autoclave and

heated at 170 °C for 2 h. **After the reaction**, 50 mg of NaNO<sub>3</sub> was added to the mixture and heating to 170 °C for another 2 h. The product was then centrifuged, washed with anhydrous ethanol and deionized water, and freeze-dried to obtain a powder sample. **The sample** was annealed at 400 °C for 2 h under argon atmosphere to obtain the final product.

### **Preparation of FeOOH**

FeOOH was prepared using the methods reported in the literature.<sup>[59]</sup> Typically, 1 mmol of FeCl<sub>3</sub>·6H<sub>2</sub>O and 3 mmol of NH<sub>4</sub>HCO<sub>3</sub> were dissolved in 40 ml of anhydrous ethanol. Then the mixed solution **was stirred** for 8 h. The product was centrifuged and **washed with** deionized water and dried in a vacuum oven at 40 °C for 12 h.

### **Calculation**

Geometric relaxations and electronic structure calculations were performed by using the projector augmented wave (PAW) pseudopotentials as implemented in the Vienna ab initio Simulation Package (VASP). Exchange correlation interactions were described by the Perdew-Burke-Ernzerhof (PBE) generalized gradient approximation (GGA). The plane wave kinetic energy was set to be 500 eV. Atomic positions and lattice parameters were fully relaxed at the GGA level until the atomic forces were smaller than 0.01 eV/Å.

### **Material characterization**

The crystalline structure of the as-obtained material was characterized by **powder** X-ray diffraction pattern (XRD, Rigaku D/Max-2400, Cu-K $\alpha$  radiation,  $\lambda = 0.15405$  nm), X-ray photoelectron spectrum (XPS, ESCALAB250x). Surface morphology and

microstructure were investigated through Field emission scanning electron microscope (FESEM, JSM 6701F) and transmission electron microscope (TEM, JEOL 2100 FEG).

### **Electrochemical surface enhancement in situ Raman**

The **electrochemical** test was performed in three-electrode system. During the in-situ Raman test, we used a transparency organic glass vessel as electrochemical test cell.<sup>[56]</sup> The saturated calomel electrode was used as the reference electrode, and a platinum electrode was used as the counter electrode.

### **OER test**

**Firstly, the catalyst ink** was prepared by dispersing 5 mg active material in the mixture solution of 2 mL deionized water, 500  $\mu$ L isopropanol and 50  $\mu$ L **Nafion**. Then a pipette was employed to remove 30  $\mu$ L of the mixture solution and placed it on the glassy carbon electrode. The OER test was performed in three-electrode system under the program of LSV with a scan rate of 5  $\text{mV s}^{-1}$  and a voltage window of 0 to 1.8 V. The glassy carbon was used as the working electrode, the saturated calomel electrode as the reference electrode, and a platinum electrode as the counter electrode.

### **Electrochemical tests**

CV and EIS were performed via an electrochemical workstation (CHI660D, Chenhua, Shanghai, China). Firstly, the active material, conductive graphite and polytetrafluoroethylene (PTFE) were mixed by a mass ratio of 85:10:5 with the help **of ethanol**. **The slurry** was uniformly coated on the carbon cloth with an area of 1  $\text{cm}^2$ . Finally, the electrodes were dried in a vacuum oven at 110  $^{\circ}\text{C}$  for 12 h and then

compressed in a tablet press. The electrochemical measurements were performed in a three-electrode system with pH-adjustable Na<sub>2</sub>SO<sub>4</sub> electrolytes. The NMO-NDs@NG material, platinum foil, and saturated calomel electrode were used as the working electrode, counter electrode and reference electrode, respectively. The electrochemical performance of NMO-NDs@NG//FeOOH hybrid SC was performed in a standard Swagelok two electrode cell. Both the positive and negative electrodes were prepared with the same coating process as mentioned above. The loading mass of the electrodes for NMO-NDs@NG and FeOOH were 1 and 0.5 mg, respectively. The average specific capacity was calculated according to the cyclic voltammogram curve using the following equation:<sup>48, 49</sup>

$$C = \frac{I}{s \cdot m} \int_{V_0}^{V_0 + \Delta V} i dV \quad (C \text{ g}^{-1}) \quad (1)$$

where  $C$  is the specific capacity ( $C \text{ g}^{-1}$ ),  $s$  indicates the scan rate ( $V \text{ s}^{-1}$ ),  $m$  stands for the mass of active material,  $\Delta V$  means the voltage window (v),  $V_0$  is the minimum voltage,  $i$  represents the current (A).

The energy density ( $E$ ) and power density ( $P$ ) was calculated according to the following formula:<sup>31</sup>

$$E = \frac{\int_{t_1}^{t_2} V \cdot I \cdot t \, dt}{3.6} \quad (W \text{ h kg}^{-1}) \quad (2)$$

$$P = \frac{3600 E}{\Delta t} \quad (W \text{ kg}^{-1}) \quad (3)$$

where  $V$  stands for the voltage window (v),  $I$  represents the current density ( $A \text{ g}^{-1}$ ),  $t_1$



means the fully discharged time (s),  $t_2$  means the fully charged time (s),  $t$  is the time (s),  $\Delta t$  indicates the discharge time (s).

## Results and Discussion

### Synthesis and characterization of **positive electrode** materials

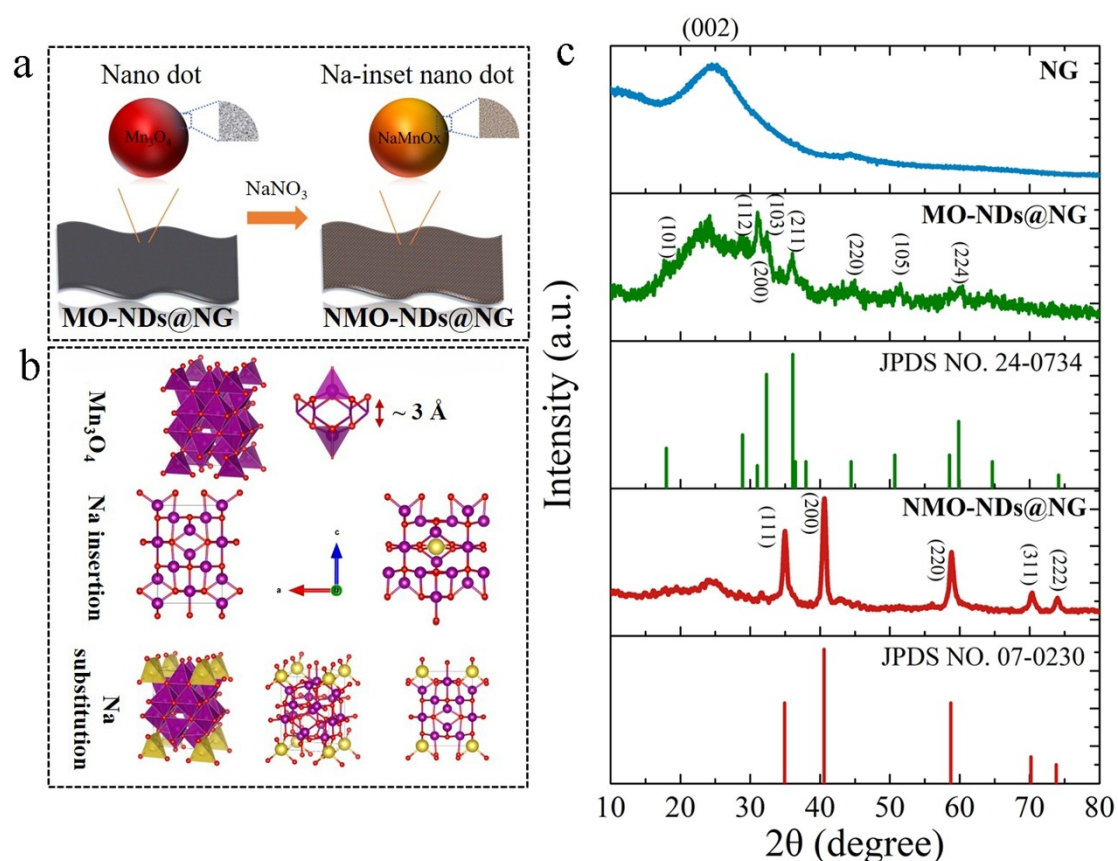


**Figure 1.** (a) **Illustration** of the fabrication procedure of NMO-NDs@NG. (b) Computational simulations of possible Na<sup>+</sup> embedded forms. Color code: oxygen (red); manganese (purple); sodium (yellow). (c) XRD patterns of NG, MO-NDs@NG and NMO-NDs@NG.

**As shown** in Figure 1a, the NMO-NDs@NG composite material was prepared by a two-step solvothermal method. Firstly, the Mn<sub>3</sub>O<sub>4</sub> nano-dots (NDs) loaded graphene

sheets were synthesized using manganese carbonyl ( $\text{Mn}_2(\text{CO})_{10}$ ) and graphene oxide (GO) as reported previously,<sup>50</sup> and the obtained product was denoted as MO-NDs@NG. The synthesis process at the atomic level enabled the MO-NDs tightly bond with graphene, and exhibited good stability. Thereafter, sodium nitrate was served as sodium precursor and reacted with MO-NDs@NG during the second solvothermal process. Ultimately, the obtained final product was denoted as NMO-NDs@NG.

The density function theory (DFT) was performed to theoretically explore the structural change of NMO-NDs@NG before and after sodium intercalation. As shown in Figure 1b,  $\text{Mn}_3\text{O}_4$  was a spinel structure with a maximum pore size of 3 Å. Na atoms preferentially substitute Mn atoms of Mn-O bonds in tetrahedron, which led to the volume shrink of  $\text{Mn}_3\text{O}_4$  lattice because of the smaller size of Na (1.91 Å). Meanwhile, the overall configuration shrink was about 2% volumetric after Na insertion, and the average valance state of Mn was reduced by 1.1%. As shown in Figure 1c, the X-ray diffraction pattern (XRD) characterization illustrated the change of the crystalline structure of MO-NDs@NG before and after sodium intercalation. The broad and weak peak (002) located at around  $24.5^\circ$  suggested the existence of graphene. Besides, the interplanar spacing (0.36 nm, calculate by Bragg equation) was a little broader than that of common graphene ( $26.5^\circ$ , 0.34 nm),<sup>51, 52</sup> which attributed to the presence of oxygen containing groups and nitrogen atom doping.<sup>53</sup> Before Na insertion, the XRD pattern for the MO-NDs@NG sample can be index to the spinel structure of  $\text{Mn}_3\text{O}_4$  (JCPDS NO. 24-0734) combining with NG. After Na insertion, all

diffraction peaks of  $Mn_3O_4$  disappeared and the new XRD pattern could be indexed to the  $Mn_2O_3$  (JPDs NO. 07-0230), indicating the successful synthesis of NMO-NDs@NG. The average crystallite size calculated by Debye-Scherrer equation from wide-angle XRD pattern was 9.625 nm.

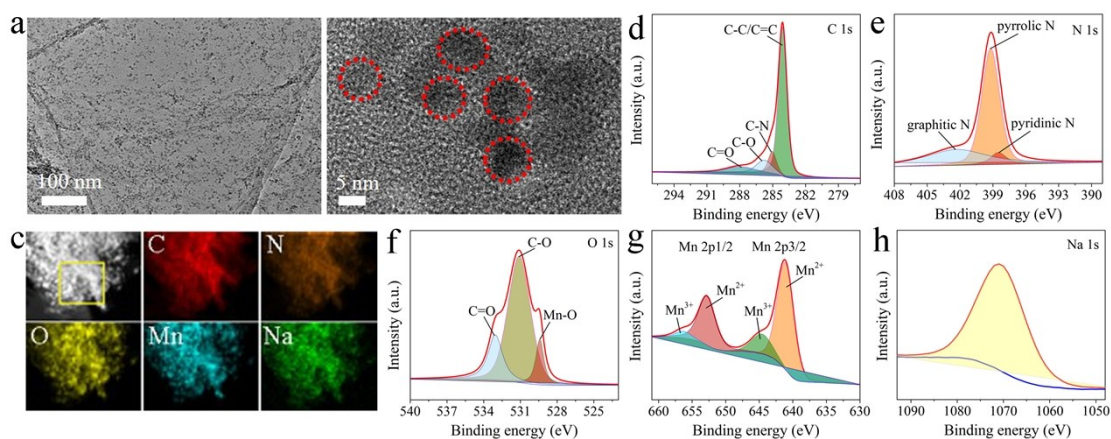


**Figure 2.** (a, b) TEM images of NMO-NDs@NG. (c) STEM image of NMO-NDs@NG with corresponding EDS elemental mappings of C, N, O, Mn and Na. High-resolution (d) C 1s, (e) N 1s, (f) O 1s, (g) Mn 2p and (h) Na 1s XPS spectra for NMO-NDs@NG.

The morphology of graphene, MO-NDs@NG and NMO-NDs@NG was investigated by the field emission scanning electron microscope (FESEM) and transmission electron microscope (TEM). From SEM and TEM images (Figure S2), the typical 2D structure of graphene was well maintained after the first-step solvothermal reaction. In Figure S3,  $Mn_3O_4$  NDs were uniformly dispersed on the surface of NG sheets with an average size of 6.75 nm after the first-step solvothermal process. Notably, as shown in Figure 2a and b, there was no obvious change observed

in the surface morphology or the particle size of the final NMO-NDs@NG product. The statistical size distribution of NMO-NDs by nano measurer software was 9.33 nm (Figure S4). And the size from XRD data was well matched with TEM data. A representative scanning transmission electron microscopy (STEM) image of NMO-NDs@NG and corresponding energy-dispersive X-ray spectroscopy (EDS) elemental mapping for C, N, O, Mn and Na elements were shown in Figure 2c. It can be clearly seen that all the elements were distributed homogenously, suggesting that Na<sup>+</sup> intercalation was uniform during the second-step solvothermal process.

XPS was employed to check the surface compositions of NMO-NDs@NG. As shown in Figure 2d, C 1s core-level spectrum exhibited four fitted peaks at 287.9, 285.8, 285.1, and 284.1 eV, which belonged to C=O, C-O, C-N, and C-C/C=C bonds, severally. The high-resolution XPS spectrum of N 1s possessed three subpeaks situated at 402.3, 399.2 and 398.4 eV (Figure 2e), which were attributed to graphitic N, pyrrolic N and pyridinic N. Since doped N can contribute more electrons to the  $\pi$ -conjugated system, and pyrrolic N was a good electron donor, graphene had high charge mobility to accelerate the electron-transfer reactions, thus N-doping can improve the overall electrical conductivity.<sup>54</sup> In addition, due to the presence of pyrrolic N and pyridinic N, more defects can be produced.<sup>55</sup> In Figure 2f, the fitted three subpeaks of O 1s spectrum attribute to C=O, C-O and Mn-O-C at 533, 531.1 and 529.4 eV, separately. The NMO-NDs were bonded to graphene by metal-oxide (Mn-O) bonding. Thus, the NMO-NDs@NG exhibited a stable structure which were not easy to fall off from graphene. As shown in Figure 2g, two major peaks of Mn

$2p_{1/2}$  and  $Mn\ 2p_{3/2}$  at 652.9 and 641.2 eV were ascribed to  $Mn^{2+}$  oxidation state. The presence of Na was confirmed by the XPS result shown in Figure 2h, suggesting that  $Na^+$  ions were successfully embedded in manganese oxide during the second-step solvothermal process.

### Effect of pH adjustment on electrochemical performance

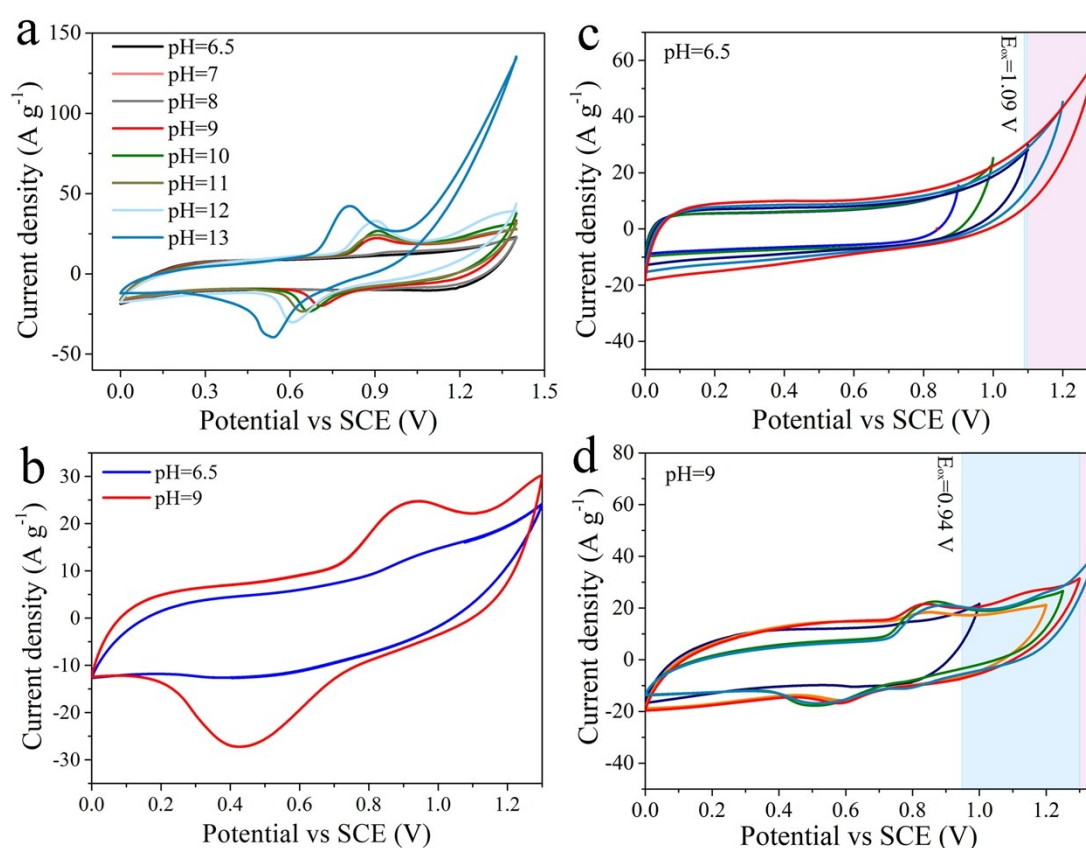


**Figure 3.** (a) CV curves of NMO-NDs@NG in electrolytes of different pH values at 50 mV s<sup>-1</sup>. (b) Comparison of CV curves (50 mV s<sup>-1</sup>) for NMO-NDs@NG at electrolytes of pH=6.5 and pH=9. (c) The CV curves and thermodynamic oxygen overpotentials of NMO-NDs@NG at different voltage windows in the electrolyte of pH=6.5 at 50 mV s<sup>-1</sup>. (d) The CV curves and thermodynamic oxygen overpotentials of NMO-NDs@NG at different voltage windows in the electrolyte of pH=9 at 50 mV

s<sup>-1</sup>.

The electrochemical performance of NMO-NDs@NG was investigated in a three-electrode system with a series of pH-controlled aqueous Na<sub>2</sub>SO<sub>4</sub> solutions as the electrolytes. As discussed above, the pH of electrolyte was an indicator of the concentration of H<sup>+</sup> and OH<sup>-</sup>, which played a pivotal role in H<sup>+</sup> and OH<sup>-</sup> involved redox reactions. In this sense, some faradic redox reactions and electrolyte decomposition including HER and OER were heavily influenced by the pH value of electrolyte. In this work, 0.1 M KOH solution was employed to adjust the pH of the 1M Na<sub>2</sub>SO<sub>4</sub> electrolyte. The voltage window of NG was 0~1 V in Na<sub>2</sub>SO<sub>4</sub> electrolyte (Figure S5). At first, in order to define suitable voltage window of the NMO-NDs@NG, cyclic voltammogram (CV) tests of NMO-NDs@NG in Na<sub>2</sub>SO<sub>4</sub>-based electrolytes at different pH values were carried out in Figure 3a. The CV curves revealed that with the increase of the pH value, a series of redox peaks appeared gradually. The maximum voltage window can be stabilized at 1.3 V when the pH of electrolyte was adjusted to 9. Later, as the pH value was further promoted, excessive hydroxide caused the shift of oxidation peak to more negative potential accompanied by the polarization at 1.3 V (Figure S6a-h). Obviously, the potential of the anodic and cathodic redox peaks both showed a descent in the electrolyte of pH=9, this was due to the fact of the elevated hydroxyl activity and the participation of hydroxyl in the capacitive behavior (Figure S6i). Moreover, NMO-NDs@NG showed a narrow voltage window of 0~0.5 V in KOH electrolyte and exhibited a battery-like energy

storage behavior mainly associated with the reactivity of OH<sup>-</sup> ions in Figure S7.

Figure 3b displayed the comparison of CV curves in the electrolytes of pH=6.5 and pH=9. It was evident that there was a pair of redox peaks in the electrolyte of pH=9, which proved that hydroxyl groups undoubtedly participated in the redox reaction on the electrode surface and increased the capacity. When the pH of the electrolyte was 6.5, the voltage window of the NMO-NDs@NG was about 0-1.1 V while the theoretical thermodynamically stable oxygen evolution potential ( $E_{ox}$ ) was 1.09 V (Figure 3c). The approximately rectangular shapes of CV indicated that such NMO-NDs@NG exhibited capacitance-dominant behavior in this electrolyte. In comparison, when the pH of the electrolyte was adjusted to 9, the stable voltage window of NMO-NDs@NG reached 0-1.3 V with  $E_{ox}$  of 0.94 V (Figure 3d). Here,  $E_{ox}$  can be calculated from Nernst equation:  $E_{ox}=1.23-0.059pH+0.244$ , which gave an explanation that the voltage window of electrode was related to the adjacent ion concentration.<sup>56</sup>  $E_{ox}$  was the theoretical electrode surface oxygen evolution potential (saturated calomel electrode relative to standard hydrogen electrode potential), and it should be pointed out that  $E_{ox}$  was also defined as the stable potential given by the thermodynamics specifically.



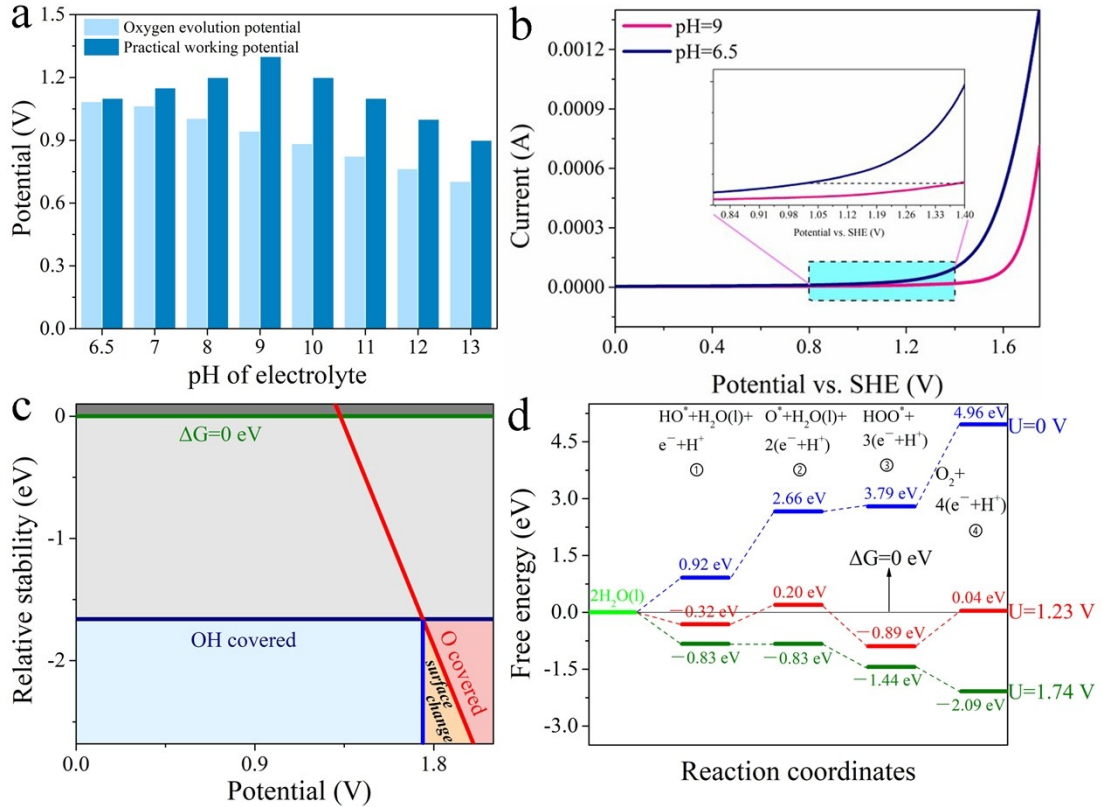


**Figure 4.** (a) The oxygen evolution potential calculated based on Nernst equation and the practical working potential of NMO-NDs@NG in the electrolytes with pH values varying from 6.5 to 13. (b) Linear sweep voltammetry (LSV) curves of NMO-NDs@NG in  $\text{Na}_2\text{SO}_4$ -based electrolytes of pH=6.5 and pH=9. (c) The phase-diagram of NMO(100) surface calculated as function of potential. (d) The free energies for water splitting steps at different potentials ( $U=0$ , 1.23 and 1.74 V) on surface of NMO predicted from DFT calculation.

Figure 4a summarized the calculated oxygen evolution potential based on the Nernst equation and the practical working potential of NMO-NDs@NG in the electrolytes with the pH values varying from 6.5 to 13. It was noting that such  $E_{ox}$  ignores the dynamics in actual electrode reaction. When the pH of the electrolytes



increased from 6.5 to 9, the oxygen evolution overpotential inevitably deviated from the ideal  $E_{ox}$ . Therefore, the oxygen evolution overpotential of the electrode increased from 0.01 to 0.36 V. From the comparison between the two electrolytes, it can be concluded that when the pH increased from 6.5 to 9, the oxygen evolution potential changed from 1.1 to 1.3 V. In addition, linear sweep voltammetry (LSV) tests (Figure 4b) of NMO-NDs@NG in the two electrolytes also confirmed that mild alkaline electrolyte was able to inhibit the occurrence of OER, thereby causing the positive potential shift. By comparing LSV curves of MnO<sub>2</sub> and NG as shown in Figure S8, the two electrodes both showed wide oxygen evolution overpotentials. The results above fully demonstrated that the pH-regulation of electrolytes could effectively expand the working voltage window of NMO-NDs@NG. Furthermore, the relative stability of NMO(100) surface as a function of potential ( $U$ ), obtained from the DFT calculations, is shown in Figure 4c. There were two reaction intermediates on the surface of coordinately unsaturated site (CUS): oxygen (O<sup>\*</sup>) occupied and hydroxyl (HO<sup>\*</sup>) occupied. Within the potential range from 1.3 to 1.9 V, the HO<sup>\*</sup>-covered and O<sup>\*</sup>-covered surfaces were stable. At a potential of 1.74 V, the surface changed from being totally HO<sup>\*</sup>-covered surface to becoming O<sup>\*</sup>-covered. The free energies of the intermediates on water splitting at various potentials are shown in Figure 4d. At the zero potential, all the water splitting steps were endothermic and energetically unfavorable (Table S1). Notice that at equilibrium potential of 1.23 V, all reaction steps became downhill in free energy, but the second and third reaction steps were endothermic. With an overpotential of 0.51 V, all reaction steps were down-hill in

free energy and become exothermal. At the rate-determining step, the activation energy was substantially higher and thus OER was intrinsically difficult on the NMO-NDs@NG surface.<sup>57</sup>

As shown in Figure S9, the Nyquist plot in electrolyte of pH=9 showed a low ion transport resistance and a sharp rise of the imaginary component of impedance at low frequencies, demonstrating the capacitive behavior. This potential region corresponded to a capacitance originating from diffusion-limited processes.<sup>58</sup> Moreover, although the two Nyquist plots tended to overlap at high frequencies, the Nyquist plot at the electrolytes of pH=6.5 showed an increase of the 45-degree linear part and a less steep slope in the low-frequency. This correlated with the irreversible reactions due to the too wide voltage window. The electrochemical impedance spectroscopy (EIS) collected under the limited potential to 1.3 V further implied that NMO-NDs@NG electrode was able to perform stably in the electrolyte of pH=9.

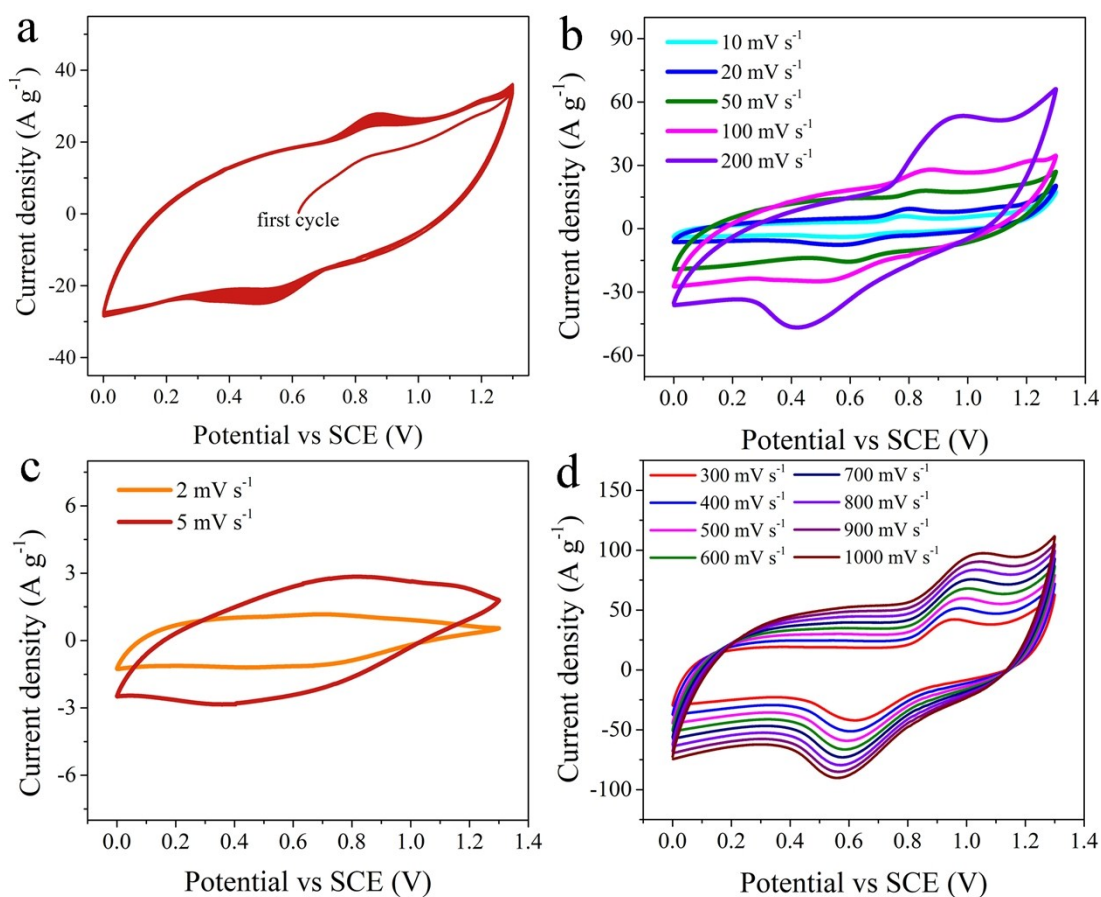


**Figure 5.** (a) **First CV** cycle of NMO-NDs@NG in the electrolyte of pH=9 at 100 mV s<sup>-1</sup>. CV curves of NMO-NDs@NG in the electrolyte with pH of 9 **at scan rates of:** (b) 10 to 200 mV s<sup>-1</sup>, (c) 2 and 5 mV s<sup>-1</sup> and (d) 300 to 1000 mV s<sup>-1</sup>.

As shown in Figure 5a, the electrode can be stabilized at 1.3 V when tested directly in electrolyte of pH=9 without any Na<sup>+</sup> ions implantation procedure that reported in literatures.<sup>24, 28, 31</sup> Figure 5b was the CV curves (0-1.3 V) of NMO-NDs@NG at scan rates range from 10 to 200 mV s<sup>-1</sup> in the electrolyte of pH=9. Two pairs of redox peaks can be clearly observed from the CV curves with an oxidation peak appearing at around 1.2 V specially. **Hydrolysis of the electrolyte was avoided by such reversible high-potential oxidation peaks**, thereby stabilizing the **voltage window** at

1.3 V. Based on the CV curves of NMO-NDs@NG in Figure 5b, the specific mass capacity were calculated to be 365.3 C g<sup>-1</sup> at 10 mV s<sup>-1</sup> and 260 C g<sup>-1</sup> at 200 mV s<sup>-1</sup>, respectively. The rate capability of NMO-NDs@NG was higher than 71%. Figure 5c showed the CV curves of the NMO-NDs@NG at scan rates of 2 mV s<sup>-1</sup> and 5 mV s<sup>-1</sup> with no polarization phenomenon at 1.3 V, indicating it had good stability even at extremely low scan rates. Moreover, in Figure 5d, the NMO-NDs@NG showed excellent rate performance, even at a large scan rate of 1000 mV s<sup>-1</sup>, the shape of the CV curve did not change significantly.

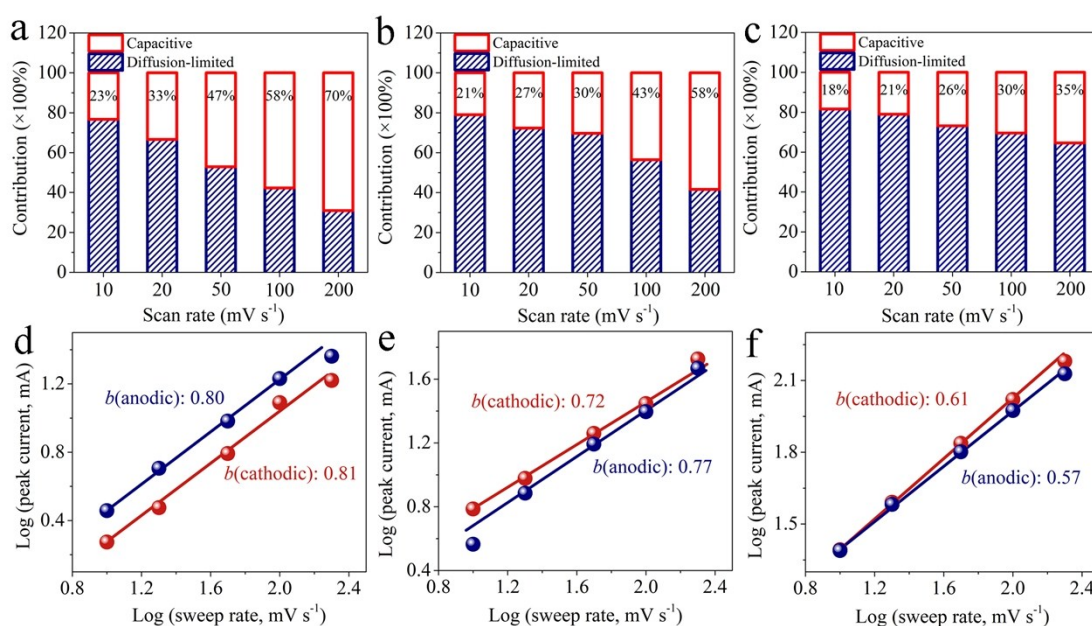


**Figure 6.** Contributions from the surface capacitive and diffusion-controlled behavior to the total stored charge of NMO-NDs@NG at different scan rates in the electrolytes with different pH values: (a) pH=6.5, (b) pH=9 and (c) pH=13. *b*-value determination: (d) the relationship between the current at 0.6 V and the scan rate in the electrolyte of pH=6.5; the relationship between the peak current and the scan rate in the electrolyte of (e) pH=9 and (f) pH=13.

Here, the electrochemical kinetic analysis was carried out to explore deep insight into the **capacitive charge storage** and diffusion-controlled process of the NMO-NDs@NG electrode.<sup>59-61</sup> According to  $i(v) = k_1v + k_2v^{1/2}$ ,<sup>42, 60</sup> where  $i(v)$ ,  $k_1v$ ,  $k_2v$  and  $v$  were the current at a fixed potential, surface-controlled and diffusion-controlled currents and scan rate, respectively. The quantitative contribution of non-diffusion limited charges involved in the process at a certain scan rate can be determined by calculating the value of  $k_1$ . By plotting  $v^{1/2}$  versus  $i(v)/v^{1/2}$ ,  $k_1$  can be obtained from the slope of the straight line. As shown in Figure 6a, especially at high scan rates, the proportion of surface capacitive contribution was much more than the diffusion-controlled contribution in the electrolyte of pH=6.5. While the diffusion-controlled contributions held dominant position when the **pH of electrolyte** was regulated to 13 in the whole range of scan rates (Figure 6c). In the electrolyte of pH=9 (Figure 6b), **both** the surface capacitive and diffusion-controlled **contributions retained** the same variation tendency as those in the electrolyte of pH=6.5 with a little decrease for surface-controlled part. The results can be explained that the local environment of ions in the solution **determined** the ions transfer tendency. Moreover, the interfacial **ions** transfer in the electrolyte of pH=6.5 was faster than that taken place in the electrolytes of pH=9 and 13. Obviously, the current tended to be proportional to the scan rate in the electrolytes of pH=6.5. In contrast, it deviated from the linear relationship in the electrolyte of pH=13 due to the dominant role of the diffusion-controlled contributions. As for the electrolyte with pH=9, owing to the existence of

appropriate amount of hydroxyl groups (that will bring out additional redox reaction, and the reaction mechanism will be explained in the following section of Operando Raman Analysis), the surface capacitive contribution and diffusion-controlled contribution coexisted in the system, and the later was stronger than that in the electrolyte of pH=6.5.

By analyzing the relationship between the current  $i$  and the scan rate  $\nu$  ( $i$ - $\nu$  curves for  $b$ -value determination,  $i=av^b$ , where  $a$  and  $b$  are constant<sup>62, 63</sup>), the degree of charge contributions from diffusion-controlled and surface capacitive behavior was qualitatively identified. As shown in Figure 6d, the NMO-NDs@NG electrode presented a fast surface-controlled process where  $b$  values at cathodic and anodic peaks were 0.81 and 0.80 in electrolyte of pH=6.5. While in Figure 6f, the NMO-NDs@NG electrode exhibited a typical diffusion-dominated process where  $b$  value at cathodic and anodic peaks were 0.61 and 0.57 in electrolyte of pH=13. In addition, in Figure 6e, the  $b$  values at cathodic and anodic peaks were 0.72 and 0.77 in electrolyte of pH=9, indicating the co-occurrence of the diffusion and surface controlled processes.<sup>64, 65</sup>

### **Energy storage mechanism of NMO-NDs@NG**

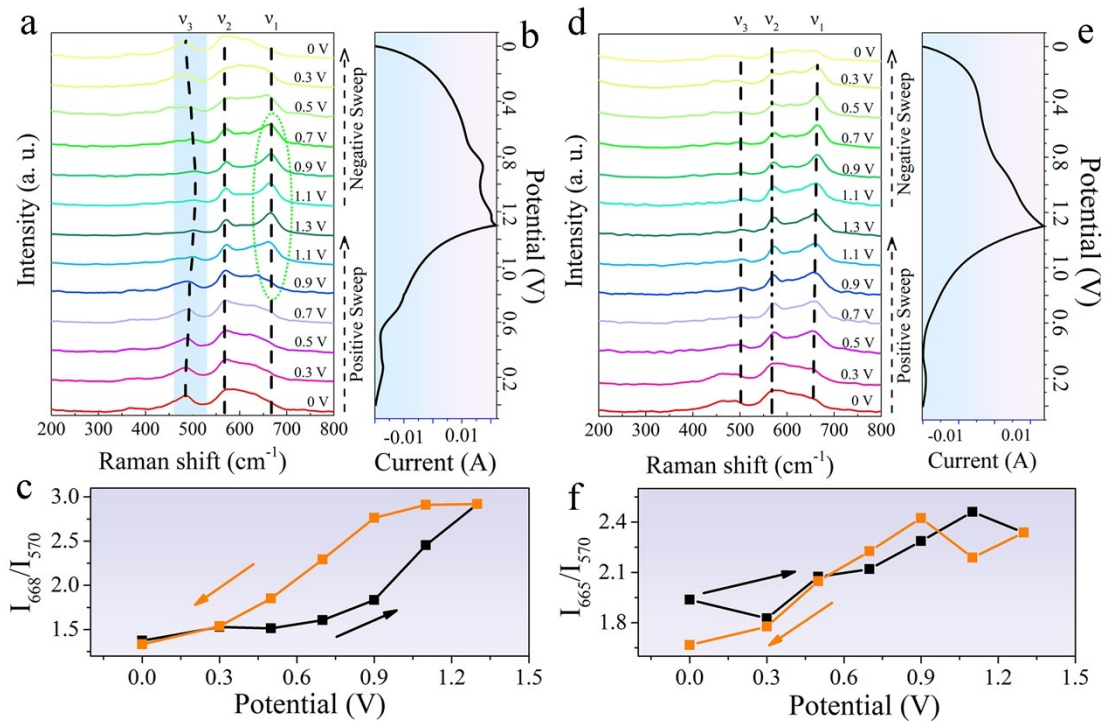


**Figure 7.** (a) Surface-enhanced in-situ electrochemical Raman spectra of NMO-NDs@NG in the electrolyte of pH=9, (b) corresponding charging and discharging curves and (c) the relationship between the voltage and intensity ratio ( $I_{668}/I_{570}$ ). (d) Raman spectra of NMO-NDs@NG in the electrolyte of pH=6.5, (e) charging and discharging curves and (f) the relationship between the voltage and intensity ratio ( $I_{665}/I_{570}$ ).

Electrochemical in-situ Raman was a surface sensitive technique in evaluating the microstructure information and the interface behavior of the working electrode.<sup>66</sup> In order to explore the reason why the hydroxyl ions in electrolyte was able to affect the related energy storage behavior of NMO-NDs@NG, the surface enhanced in-situ electrochemical Raman measurement was carried out in the electrolytes of pH=6.5 and pH=9. The NMO-NDs@NG electrode surface was coated with gold to enhance

the strength of surface signals (Figure S10), and the voltage window varied from 0 to 1.3 V with the scan rate of 2 mV s<sup>-1</sup>. As shown in Figure S11, there were three major Raman regions: 660-670 cm<sup>-1</sup> ( $\nu_1$ ), 569-577 cm<sup>-1</sup> ( $\nu_2$ ) and 485-507 cm<sup>-1</sup> ( $\nu_3$ ),<sup>67-69</sup> where  $\nu_1$ ,  $\nu_2$  and  $\nu_3$  represent the Mn-O stretching vibrations of [MnO<sub>6</sub>] octahedra.<sup>66, 70</sup> Moreover, the peak located at 980 cm<sup>-1</sup> was ascribed to SO<sub>4</sub><sup>2-</sup>, and no obvious change occurred during the electrochemical cycling process. The adsorption/desorption of Na<sup>+</sup> ions during charging/discharging process will affect the stretching vibration largely of the  $\nu_1$  (Mn-O) along d<sub>z</sub><sup>2</sup> of [MnO<sub>6</sub>]. Na<sup>+</sup> ions actually had no obvious influence on the stretching vibration in the basal plane of [MnO<sub>6</sub>] ( $\nu_2$  (Mn-O) along (d<sub>x<sup>2</sup>-y<sup>2</sup>) of [MnO<sub>6</sub>]) (Figure S12). Moreover, OH<sup>-</sup> ions in electrolyte affected scarcely the Raman signals at high wavenumber range (Figure S13).</sub>

As shown in Figure 7a, in the electrolyte of pH=9, as the voltage increased from 0 to 1.3 V (Figure 7b), the intensity of  $\nu_1$  (Mn-O) band significantly increased due to the deintercalation of Na<sup>+</sup> ions. Besides, the distortion of intrinsic crystal space lattice that was transformed from monoclinic structure to hexagonal phase led to the intensity enhancement of  $\nu_2$  (Mn-O) band. Such transformation can be explained by the shorter Mn-O bond of the [MnO<sub>6</sub>] and the oxidation of Mn(III). Figure 7c displayed the proportion of peak intensity of  $\nu_1$  (Mn-O) to  $\nu_2$  (Mn-O) that was closely associated with the charge storage mechanism toward Na<sup>+</sup> adsorption/desorption on the surface of NMO-NDs. During charging process, the intensity ratio of  $I_{\nu_1(Mn-O)}$  and  $I_{\nu_2(Mn-O)}$  (denoted as  $I_{668}/I_{570}$ ) revealed the desorption process of Na<sup>+</sup> ions from NMO-NDs. Likewise, a blue shift from 485 to 507 cm<sup>-1</sup> occurred in this charging process can be



detected in the  $\nu_3$  (Mn-O) stretching band, which further suggested the  $\text{Na}^+$  ions extraction. This process mainly attributed to the oxidation-state changes of Mn ions and the increase of the force between the  $[\text{MnO}_6]$  octahedral crystal planes. In addition, the oxidation-state change was accompanied by the strong interaction of  $\text{OH}^-$  ions in the oxygen vacancies of trivalent manganese.<sup>66</sup> When the applied voltage decreased from 1.3 to 0 V, due to the intercalation of  $\text{Na}^+$  ions along with the reduction of  $\text{OH}^-$  ions, a redshift of the  $\nu_3$  (weak vibration mode of Mn-O bond) peak from 507 to 484  $\text{cm}^{-1}$  was observed, and the force between the  $[\text{MnO}_6]$  octahedral crystal planes was weakened. Through Lorentz fitting, the peaks at 485-507  $\text{cm}^{-1}$  represent the low-valence  $\text{Mn}^{2+}/\text{Mn}^{3+}$ , while the peaks near 575  $\text{cm}^{-1}$  indicated the high-valence  $\text{Mn}^{4+}$  (Figure S14). A small peak located at 367  $\text{cm}^{-1}$  corresponded to  $\text{MnOOH}$  or  $\text{Mn}_2\text{O}_3$  in Figure 7a. In addition, when the voltage increased from 0 to 0.9 V, a new peak appeared in the  $\nu_1$  band at around 670  $\text{cm}^{-1}$ , which was related to the generation of intermediate products associated with  $\text{Mn}^{3+}$ . Besides, the redox peak positioned at about 0.9 V in CV curves (Figure 7b and Figure 5b) corresponds to the redox reaction of Mn(III) ions under the presence of adsorbed  $\text{OH}^-$  ions due to the strong adsorption energy on the oxygen vacancies of Mn(III). Therefore, it can be confirmed that the synergistic effects of  $\text{Na}^+$  ions and  $\text{OH}^-$  ions made a cooperative contribution for the NMO-NDs@NG.

In the electrolyte of pH=6.5, no obvious change occurred in the intensity of  $\nu_2$  (Mn-O) band (Figure 7d) during charge/discharge process (Figure 7e). Importantly, as shown in Figure 7d, the intensity of  $\nu_1$  (Mn-O) band was varied slightly with the

alteration of the potential. The calculated intensity ratio of  $I_{665}/I_{570}$  was summarized in Figure 7f, and the relatively gentle slope of the **curve** reflected the fact that only a small amount of  $\text{Na}^+$  participated in the relevant reaction compared to that in the electrolyte of pH=9. Besides, there was no significant blue shift in the  $\nu_3$  band in the electrolyte of pH=6.5 (Figure 7d). In Figure 7f, it can be observed that although the initial ratio of  $I_{665}/I_{570}$  was the same as that in pH=9, a lower ratio was obtained **at the maximum potential**. Moreover, when **discharging** to 0 V, the value of  $I_{665}/I_{570}$  did not return to the initial position due to **the polarization** caused by irreversible reaction. Thus, the  $\text{Na}^+$  ions **made** a primary capacitance contribution for the NMO-NDs@NG electrode in the electrolyte of pH=6.5.

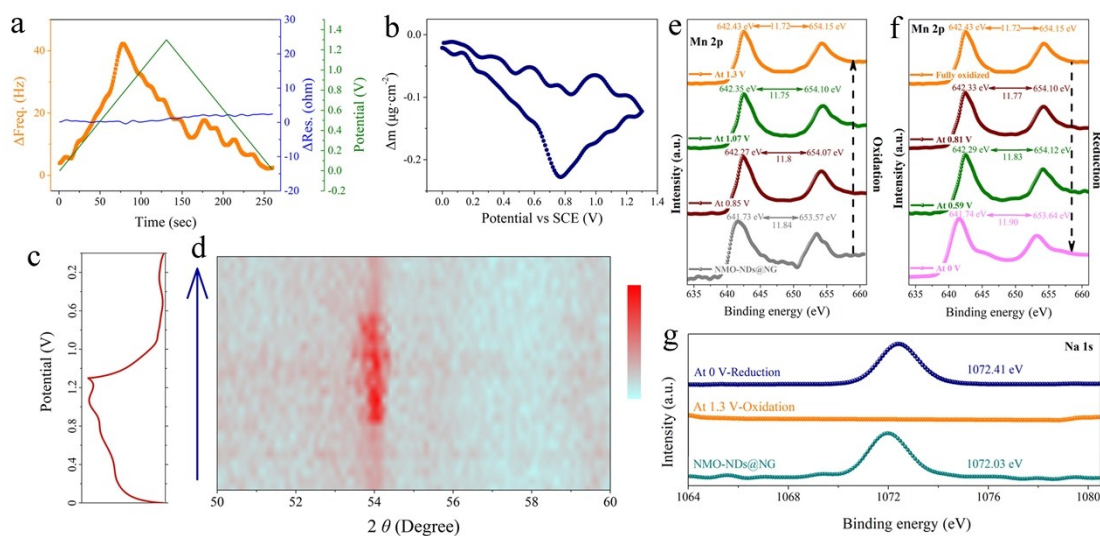


**Figure 8.** EQCM analysis of NMO-NDs@NG: (a)  $\Delta Freq.$ ,  $\Delta Res.$  and the potential change as function of time during the entire charge-discharge cycle. (b)  $\Delta m$  as a function of potential. (c) The charging and discharging curves and (d) the corresponding in-situ XRD contour plot of NMO-NDs@NG in the electrolyte of pH=9. Mn 2p core-level XPS spectra of the NMO-NDs@NG electrode at different

charge (e) and discharge (f) states. (g) Na 1s core-level XPS spectra of the NMO-NDs@NG electrode at different charge and discharge states.

To obtain a deeper understanding of energy storage mechanism of NMO-NDs@NG, electrochemical quartz crystal microbalance (EQCM) measurement was carried out. The raw EQCM data were shown in Figure S15. NMO-NDs@NG electrodes were prepared by vacuum filtration-and-transfer (VFT) method, and then conducted gravimetric EQCM measurement in 1 M Na<sub>2</sub>SO<sub>4</sub> (pH=6.5) electrolyte. Figure S16a was the raw EQCM data for the VFT coating electrode, the resonance resistance was nearly unchanged and meet the application of Sauerbrey equation during the electrochemical measurement. As shown in Figure S16b, the mass of the electrode continuously decreased during charging and only cation will be adsorption/desorption. Figure S16c showed the experimental ion population changes ( $\Delta\Gamma_{exp}$ ) and theoretical ion population changes ( $\Delta\Gamma_{theor}$ ) as a function of charge density ( $\Delta Q$ ). We found that when the molecular mass ( $M_i$ ) of solvated cationic was 95 g mol<sup>-1</sup>,  $\Delta\Gamma_{exp}$  and  $\Delta\Gamma_{theor}$  showed good coincidence. That was, one mole of Na<sup>+</sup> ions with four H<sub>2</sub>O molecules was absorption/desorption for every one mole of electron transfer. In the 1M KOH electrolyte, EQCM test was conducted at a scan rate of 10 mV s<sup>-1</sup>, and the voltage window was 0-0.6 V (Figure S17a). However, because of the complicated electrochemical behavior, it was difficult to accurately judge the mass changes. Figure S17b showed that mainly OH<sup>-</sup> ions were involved in the electrochemical reaction and resulted in the NMO's contraction. As the valence of

manganese increased, from III to IV, the structure of NMO was reconstructed. Thus, NMO-NDs@NG in KOH mainly reacted with OH<sup>-</sup> ions, and K<sup>+</sup> ions contribution to the capacitance was much less. In the electrolyte of pH=9, EQCM test was conducted at a scan rate of 10 mV s<sup>-1</sup>, and the voltage window was 0-1.3 V (Figure 8a). As shown in Figure 8b, the mass of the electrode firstly decreased from 0 to 0.85 V and then increased from 0.85 to 1.3 V during charging process. Thus, there will be Na<sup>+</sup> and OH<sup>-</sup> ions involved in the electrochemical reaction. According to the analytical result of in-situ Raman, Mn(III) was oxidized to Mn(IV) even to higher valence in the charging process. It can be seen from the curve of mass change that before 0.85 V, it was obvious that ions were adsorbed and desorbed on the electrode for energy storage. This showed that at low voltage, the electrode-preferred energy storage mode was similar to the energy storage behavior in the Na<sub>2</sub>SO<sub>4</sub> electrolyte. The energy storage behavior based on cation adsorption and desorption on the electrode. But above 0.85 V, the change in mass during charging had reversed. This was because OH<sup>-</sup> participated in the redox-type energy storage reaction. The valence state of manganese in NMO-NDs@NG changed, the MnO<sub>6</sub> octahedron shrank (the Raman  $\nu_3$  band changed), and the NMO structure was reset. At the same time, the change in mass also had this regularity during discharging process. This indicated that NMO-NDs@NG simultaneously performed the adsorption/desorption of Na<sup>+</sup> ions and the redox reaction of OH<sup>-</sup> ions.

In-situ XRD and ex-situ XPS tests were performed to monitor the phase evolution of the NMO-NDs@NG electrode during the first charge-discharge cycle in the

electrolyte of pH=9. As shown in Figure S18, the three-electrodes configuration was assembled for the in-situ XRD test. According to the in-situ XRD tests (Figure 8c, d), when charging to high voltage (more than 0.8 V), a new XRD diffraction peak appeared at around 54 degrees. This was because at high potential, OH<sup>-</sup> participates in further redox reactions and raised the valence of low-valence manganese to tetravalent. The internal structure of the NMO-NDs was reconstructed, and the MnO<sub>6</sub> octahedron crystal shrink at the same time. In addition, during discharging process, the peak intensity gradually decreased due to the reduction of OH<sup>-</sup> with NMO-NDs, indicating the reversibility of the reaction. Ex-situ XPS measurements were carried out on the NMO-NDs@NG electrode at different voltages on both charge and discharge processes. The Mn 2p core-level XPS spectra demonstrated oxidation and reduction of Mn during charge and discharge processes, respectively, which were associated with Na<sup>+</sup> deintercalation and intercalation. In the charging process, the interval of binding energy between Mn2p<sub>3/2</sub> and Mn2p<sub>1/2</sub> core-level was decreased from 11.84 to 11.72 eV (Figure 8e). And then increased from 11.72 to 11.90 eV during discharging process (Figure 8f). Meanwhile, Na 1s core-level XPS spectra verified the deintercalation and intercalation of Na<sup>+</sup> from the NMO-NDs@NG electrode at different states (Figure 8g). Furthermore, Mn 2p<sub>3/2</sub> core-level XPS spectra of the NMO-NDs@NG electrode at charging and discharging states showed obvious binding energy shift (Figure S19). Na<sup>+</sup> and OH<sup>-</sup> ions caused valence change with the newly emerged redox peaks and increased current density in the large voltage window of 0-1.3 V.

Moreover, the adsorption energies and energetically favorable adsorption sites of  $\text{Na}^+$ ,  $\text{K}^+$  and  $\text{OH}^-$  ions were conducted by DFT calculation (Table S2). And we had compared the adsorption state of electrolytic ions required for understanding the changes of above peak shift and peak intensity. Four kinds of adsorption configurations of  $\text{Na}^+/\text{K}^+$  ions on NMO-NDs@NG were denoted as: Na/K-top, Na/K-3fh-O, Na/K-3fh-Mn and Na/K-middle. The strong adsorption energy ( $E_{\text{ads}}$ ) illustrated the cations were more likely to adsorbed on the electrode surface.  $\text{OH}^-$  ions in alkaline electrolyte exhibited a strong  $E_{\text{ads}}$  on the oxygen vacancies of trivalent manganese (OH-O-vacancy) than on regular  $[\text{MnO}_6]$  octahedron (OH-Mn-top). This indicated the structure deformation and vacancies were more easily occurred of trivalent manganese.

## Device performance

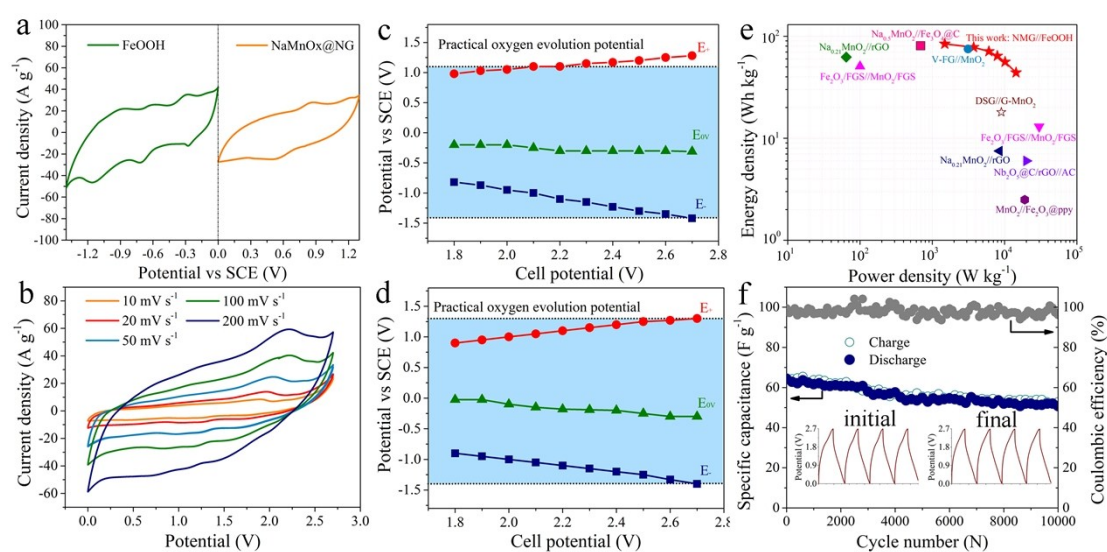


**Figure 9.** (a) CV curves of NMO-NDs@NG positive electrode (0-1.3 V) and FeOOH

negative electrode (-1.4-0 V) in the electrolyte of pH=9. (b) CV curves of NMO-NDs@NG//FeOOH hybrid SC at different scan rates with a voltage window of 2.7 V in the electrolyte of pH=9. Potential limits of positive and negative electrodes vs cell voltage during galvanostatic charge/discharge of NMO-NDs@NG//FeOOH hybrid SC in the electrolytes of pH=6.5 (c) and pH=9 (d).  $E_+$  and  $E_-$  represent the maximum and minimum potentials reached by the positive and negative electrodes, respectively;  $E_{0V}$  corresponds to the rest potential of the electrodes at cell voltage of 0 V. (e) Ragone plots of NMO-NDs@NG//FeOOH hybrid SC and the reported representative ASCs. (f) Cycling performance of NMO-NDs@NG//FeOOH hybrid SC at 2 A g<sup>-1</sup>. Insets showing the galvanostatic charge/discharge plots of the device before and after cycling.

To evaluate the effectiveness of using the pH-regulated electrolyte (pH=9) on the construction of aqueous high-voltage SC, we assembled a hybrid SC by employing NMO-NDs@NG as the positive electrode and home-made FeOOH as the negative electrode, and the as-obtained device was denoted as NMO-NDs@NG//FeOOH hybrid SC. FeOOH was served as the negative material because such material generally showed a wide voltage window in both neutral and alkaline electrolytes,<sup>71, 72</sup> and the pH trifling variation had little effect on its voltage window. Figure S20a showed the SEM image of FeOOH, which displayed a 10 μm cubic particles morphology. The amplifying SEM image (Figure S20b) revealed a structure with smaller nanoparticles on the surface of the cubic particle. Figure S21 showed the

XRD pattern, where the diffraction peaks correspond to the FeOOH (JCPDS NO. 22-0353). As shown in Figure S22a, the CV curves of FeOOH showed distinct redox peaks with a wide **voltage window** of  $-1.4-0$  V in the electrolyte of pH=9. When the **voltage window** widened to  $-1.5-0$  V, the CV curve still showed no obvious polarization phenomenon (Figure S22b).

Figure 9a **showed** the CV curves of both the positive and negative materials in the regulated  $\text{Na}_2\text{SO}_4$ -based electrolyte (pH=9). It can be seen that, the maximum voltage of the positive electrode can reach 1.3 V and the maximum voltage of the negative electrode can reach  $-1.4$  V. Besides, the **voltage window** of the assembled **hybrid SC** can achieve a high value of 2.7 V **in Figure 9b**. Notably, the negligible distortion of the CV curves even at a high scan rate of  $200 \text{ mV s}^{-1}$  indicated the small internal resistance of the device. The mass specific **capacity** of **hybrid SC** device calculated based on the CV were  $177.7 \text{ C g}^{-1}$  at  $10 \text{ mV s}^{-1}$  and  $105.6 \text{ C g}^{-1}$  at  $200 \text{ mV s}^{-1}$ , respectively.

In order to further confirm that the pH adjustment of electrolyte certainly increased the **voltage window** of the device, the potential threshold values of positive and negative electrodes of NMO-NDs@NG//FeOOH **hybrid SC** in the electrolytes of pH=6.5 and pH=9 with Hg/HgO reference were determined by galvanostatic cycling for cell **voltage** from 1.8 V to 2.7 V, respectively. The practical voltage of the positive electrode ( $E_+$ ), zero charge potential of **hybrid SC** ( $E_{0V}$ ) and the practical voltage of the negative electrode ( $E_-$ ) were monitored in real time. Here, the theoretical thermodynamically stable potential of positive electrode **was** 1.09 V in the electrolyte



of pH=6.5 as mentioned in Figure 9c, and the blue enclosed area was the stable oxygen evolution/hydrogen evolution overpotential region. Figure 9c showed the monitored result of the device in the electrolyte of pH=6.5. It can be seen that, the practical stable oxygen evolution potential of the positive electrode was about 1.1 V and the hydrogen evolution potential of the negative electrode was -1.4 V. As shown in Figure S23, the CV curves of the device using Na<sub>2</sub>SO<sub>4</sub> electrolyte of pH=6.5 under 2.7 V were strongly polarized. In contrast, as shown in Figure 9d, when the two electrodes were monitored in the electrolyte of pH=9, the practical oxygen evolution potential of the positive electrode reached 1.3 V. Thus, combining with the -1.4 V FeOOH negative electrode, the voltage window of the full device was able to reach 2.7 V.

Ragone plot of NMO-NDs@NG//FeOOH hybrid SC was summarized in Figure 9e along with a comparison of energy density towards power density with some representative aqueous ASCs reported previously, such as Na<sub>0.5</sub>MnO<sub>2</sub>//Fe<sub>3</sub>O<sub>4</sub>@C,<sup>28</sup> Na<sub>0.21</sub>MnO<sub>2</sub>//rGO,<sup>73</sup> V-FG//MnO<sub>2</sub>,<sup>48</sup> Fe<sub>2</sub>O<sub>3</sub>/FGS//MnO<sub>2</sub>/FGS,<sup>72</sup> DSG//G-MnO<sub>2</sub>,<sup>74</sup> Nb<sub>2</sub>O<sub>5</sub>@C/rGO//AC<sup>75</sup> and MnO<sub>2</sub>//Fe<sub>2</sub>O<sub>3</sub>@ppy.<sup>76</sup> The maximum energy density of our NMO-NDs@NG//FeOOH hybrid SC was 68 Wh kg<sup>-1</sup> at power density of 1423 W kg<sup>-1</sup>, which was higher than the majority of other devices shown in Figure 9e. Furthermore, in Figure 9f, after tested for 10000 cycles at 2 A g<sup>-1</sup>, the capacity retention of NMO-NDs@NG//FeOOH hybrid SC maintained about 86 % of the initial value, indicating a good cycling stability. In addition, the insets illustrated that the device could still work stably at 2.7 V after the long-term cycles.

## Conclusions

In summary, a new NMO-NDs@NG **positive electrode** material was prepared by a two-step solvothermal method, where sodium-embedded manganese oxide nano-dots are uniformly loaded on nitrogen-doped graphene sheets. Interestingly, we found that increasing the pH value of the initial neutral Na<sub>2</sub>SO<sub>4</sub> electrolyte was able to elevate the overpotential of oxygen evolution of the NMO-NDs@NG electrode and introduce additional redox reaction at the same time. It was because that the NMO-NDs@NG chiefly showed a surface-controlled pseudocapacitive behavior in the neutral electrolyte, but mainly displayed a battery-like behavior in the alkaline electrolyte. Properly increasing the pH value of the initial neutral electrolyte (pH=9), the emerging reversible redox reaction near the water decomposition potential effectively inhibited the water decomposition occurred on the electrode surface.

Through the pH-regulation strategy, the NMO-NDs@NG electrode exhibited a widened **voltage window** of 0-1.3 V in the pH-regulated Na<sub>2</sub>SO<sub>4</sub> electrolyte (pH=9) as well as a 234% increased capacity. When coupled with the home-made FeOOH particles served as the negative electrode, the as-built aqueous hybrid SC showed a wide **voltage window** of 2.7 V, and delivered a high energy density of 68 Wh kg<sup>-1</sup> as well as a high power density of 27 kW kg<sup>-1</sup>.

**The results verify the effectiveness of the pH-regulation of electrolytes for cation-intercalated manganese oxides to extend the voltage window of aqueous SCs. From the aspect of suppressing water electrolysis, the important roles of both electrolyte**

and electrode surface are very evident, as proved by this study. Also, fundamental understanding of the factors relevant to the operating voltage is conducive to provide guidance to construct better high-voltage aqueous SCs. We believe that the implementation of high-voltage aqueous SCs in industrial production is within reach and will be facilitated through further expanding their operating voltages.

### Conflict of Interest

The authors declare no conflict of interest.

### Acknowledgements

This work was supported by the National Nature Science Foundations of China (21573265, 21673263 and 21805292), One-Three-Five Strategic Planning of Chinese Academy of Sciences (CAS), and the DNL Cooperation Fund, CAS (DNL180307).

### References

1. J. R. Miller and P. Simon, *Science*, 2008, **321**, 651-652.
2. X. Yang, C. Cheng, Y. Wang, L. Qiu and D. Li, *Science*, 2013, **341**, 534-537.
3. L. L. Zhang and X. Zhao, *Che. Soc. Rev.*, 2009, **38**, 2520-2531.
4. M. Salanne, B. Rotenberg, K. Naoi, K. Kaneko, P. L. Taberna, C. P. Grey, B. Dunn and P. Simon, *Nat. Energy*, 2016, **1**, 16070.
5. T. Ling, P. Da, X. Zheng, B. Ge, Z. Hu, M. Wu, X. W. Du, W. B. Hu, M. Jaroniec and S. Z. Qiao, *Sci. Adv.*, 2018, **4**, eaau6261.
6. C. Young, W. Jie, J. Kim, Y. Sugahara and Y. Yamauchi, *Chem. Mater.*, 2018, **30**, acs.chemmater.8b00836.
7. J. Wang, J. Tang, B. Ding, V. Malgras, Z. Chang, X. Hao, Y. Wang, H. Dou,

- X. Zhang and Y. Yamauchi, *Nat. Commun.*, 2017, **8**, 15717.
8. H. Hou-Sheng, C. Kuo-Hsin, S. Norihiro, Y. Yusuke, H. Chi-Chang and W. Kevin C-W, *Small*, 2013, **9**, 2520-2526.
  9. B. P. Bastakoti, H. S. Huang, L. C. Chen, K. C. Wu and Y. Yamauchi, *Chem. Commun.*, 2012, **48**, 9150-9152.
  10. M. He, K. Fic, E. Fra, P. Novák and E. J. Berg, *Energ. Environ. Sci.*, 2016, **9**, 623-633.
  11. J. Zhang, J. Jiang, H. Li and X. Zhao, *Energ. Environ. Sci.*, 2011, **4**, 4009-4015.
  12. L. Su, S. Lei, L. Liu, L. Liu, Y. Zhang, S. Shi and X. Yan, *J. Mater. Chem. A*, 2018, **6**, 9997-10007.
  13. N. S. Choi, Z. Chen, S. A. Freunberger, X. Ji, Y. K. Sun, K. Amine, G. Yushin, L. F. Nazar, J. Cho and P. G. Bruce, *Angew. Chem. Int. Edit.*, 2012, **51**, 9994-10024.
  14. H. Sun, X. Fu, S. Xie, Y. Jiang and H. Peng, *Adv. Mater.*, 2016, **28**, 2070-2076.
  15. W. Zuo, R. Li, C. Zhou, Y. Li, J. Xia and J. Liu, *Adv. Sci.*, 2017, **4**, 1600539.
  16. K. Fic, G. Lota, M. Meller and E. Frackowiak, *Energ. Environ. Sci.*, 2012, **5**, 5842-5850.
  17. E. Raymundo-Piñero, F. Leroux and F. Béguin, *Adv. Mater.*, 2006, **18**, 1877-1882.
  18. V. Khomenko, E. Raymundo-Piñero and F. Béguin, *J. Power Sources*, 2010, **195**, 4234-4241.
  19. X. Lu, Y. Zeng, M. Yu, T. Zhai, C. Liang, S. Xie, M. S. Balogun and Y. Tong, *Adv. Mater.*, 2014, **26**, 3148-3155.
  20. M. Yu, Y. Han, X. Cheng, L. Hu, Y. Zeng, M. Chen, F. Cheng, X. Lu and Y. Tong, *Adv. Mater.*, 2015, **27**, 3085-3091.
  21. M. Yu, X. Cheng, Y. Zeng, Z. Wang, Y. Tong, X. Lu and S. Yang, *Angew. Chem. Int. Edit.*, 2016, **128**, 6874-6878.
  22. T. Zhai, X. Lu, H. Wang, G. Wang, T. Mathis, T. Liu, C. Li, Y. Tong and Y.

- Li, *Nano Lett.*, 2015, **15**, 3189-3194.
23. Q. Gao, L. Demarconnay, E. Raymundo-Piñero and F. Béguin, *Energ. Environ. Sci.*, 2012, **5**, 9611-9617.
24. W. Zuo, C. Xie, P. Xu, Y. Li and J. Liu, *Adv. Mater.*, 2017, **29**, 1703463.
25. M. Yu, D. Lin, H. Feng, Y. Zeng, Y. Tong and X. Lu, *Angew. Chem. Int. Edit.*, 2017, **129**, 5546-5551.
26. Z. Weng, F. Li, D. W. Wang, L. Wen and H. M. Cheng, *Angew. Chem. Int. Edit.*, 2013, **125**, 3810-3813.
27. J. Wang, S. P. Feng, Y. Yang, N. Y. Hau, M. Munro, E. Ferreira-Yang and G. Chen, *Nano Lett.*, 2015, **15**, 5784-5790.
28. N. Jabeen, A. Hussain, Q. Xia, S. Sun, J. Zhu and H. Xia, *Adv. Mater.*, 2017, **29**, 1700804.
29. J. Y. Hwang, M. Li, M. F. El-Kady and R. B. Kaner, *Adv. Funct. Mater.*, 2017, **27**, 1605745.
30. J. Yan, Q. Wang, T. Wei and Z. Fan, *Adv. Energy Mater.*, 2014, **4**, 1300816.
31. T. Xiong, T. L. Tan, L. Lu, W. S. V. Lee and J. Xue, *Adv. Energy Mater.*, 2018, **8**, 1702630.
32. T. Xiong, W. S. V. Lee, L. Chen, T. L. Tan, X. Huang and J. Xue, *Energ. Environ. Sci.*, 2017, **10**, 2441-2449.
33. S.-E. Chun, B. Evanko, X. Wang, D. Vonlanthen, X. Ji, G. D. Stucky and S. W. Boettcher, *Nat. Commun.*, 2015, **6**, 7818.
34. L. Suo, O. Borodin, T. Gao, M. Olguin, J. Ho, X. Fan, C. Luo, C. Wang and K. Xu, *Science*, 2015, **350**, 938-943.
35. Y. Yamada, K. Usui, K. Sodeyama, S. Ko, Y. Tateyama and A. Yamada, *Nat. Energy*, 2016, **1**, 16129.
36. M. R. Lukatskaya, J. I. Feldblyum, D. G. Mackanic, F. Lissel, D. L. Michels, Y. Cui and Z. Bao, *Energ. Environ. Sci.*, 2018, **11**, 2876-2883.
37. Q. Dou, Y. Lu, L. Su, X. Zhang, S. Lei, X. Bu, L. Liu, D. Xiao, J. Chen and S. Shi, *Energy Storage Mater.*, 2019, **23**, 603-609.
38. C. An, W. Li, M. Wang, Q. Deng and Y. Wang, *Electrochim. Acta*, 2018, **283**,

603-610.

39. H. Tomiyasu, H. Shikata, K. Takao, N. Asanuma, S. Taruta and Y. Y. Park, *Sci. Rep.*, 2017, **7**, 45048.
40. M. Yu, Y. Lu, H. Zheng and X. Lu, *Chem.–Eur. J.*, 2018, **24**, 3639-3649.
41. G. D. Short and E. Bishop, *Anal. Chem.*, 1965, **37**, 962-967.
42. A. J. Bard, L. R. Faulkner, J. Leddy and C. G. Zoski, *Electrochemical methods: fundamentals and applications*, Wiley New York, 1980.
43. H. Rubin and F. Collins, *J. Phys. Chem.*, 1954, **58**, 958-962.
44. J. Y. Luo, W. . Cui, P. He and Y. Y. Xia, *Nat. Chem.*, 2010, **2**, 760.
45. W. Li, W. R. McKinnon and J. R. Dahn, *J. Electrochem. Soc.*, 1994, **141**, 2310-2316.
46. Z. Yang, R. Gao, N. Hu, J. Chai, Y. Cheng, L. Zhang, H. Wei, E. S.-W. Kong and Y. Zhang, *Nano-Micro Lett.*, 2012, **4**, 1-9.
47. W. S. Hummers Jr and R. E. Offeman, *J. Am. Chem. Soc.*, 1958, **80**, 1339-1339.
48. T. Zhai, S. Sun, X. Liu, C. Liang, G. Wang and H. Xia, *Adv. Mater.*, 2018, **30**, 1706640.
49. D. Zheng, J. Ye, L. Zhou, Y. Zhang and C. Yu, *Electroanal.*, 2009, **21**, 184-189.
50. L. Liu, L. Su, J. Lang, B. Hu, S. Xu and X. Yan, *J. Mater. Chem. A*, 2017, **5**, 5523-5531.
51. K. H. Liao, A. Mittal, S. Bose, C. Leighton, K. A. Mkhoyan and C. W. Macosko, *ACS Nano*, 2011, **5**, 1253-1258.
52. G. Wang, J. Yang, J. Park, X. Gou, B. Wang, H. Liu and J. Yao, *J. Phys. Chem. C*, 2008, **112**, 8192-8195.
53. Z. Ma, X. Huang, S. Dou, J. Wu and S. Wang, *J. Phys. Chem. C*, 2014, **118**, 17231-17239.
54. H. M. Jeong, J. W. Lee, W. H. Shin, Y. J. Choi, H. J. Shin, J. K. Kang and J. W. Choi, *Nano Lett.*, 2011, **11**, 2472-2477.
55. Y. Liu, N. Zhang, L. Jiao and J. Chen, *Adv. Mater.*, 2015, **27**, 6702-6707.

56. C. N. Chang, H. B. Cheng and A. C. Chao, *Environ. Sci. Technol.*, 2004, **38**, 1807-1812.
57. X. Shan, D. S. Charles, Y. Lei, R. Qiao, G. Wang, W. Yang, M. Feygenson, D. Su and X. Teng, *Nat. Commun.*, 2016, **7**, 13370.
58. M. R. Lukatskaya, S. Kota, Z. Lin, M. Q. Zhao, N. Shpigel, M. D. Levi, J. Halim, P. L. Taberna, M. W. Barsoum and P. Simon, *Nat. Energy*, 2017, **2**, 17105.
59. M. Forghani and S. W. Donne, *J. Electrochem. Soc.*, 2018, **165**, A664-A673.
60. T. Brezesinski, J. Wang, S. H. Tolbert and B. Dunn, *Nat. Mater.*, 2010, **9**, 146.
61. A. J. Bard and L. R. Faulkner, *Electrochemical Methods*, 2001, **2**, 482.
62. D. Chao, C. Zhu, P. Yang, X. Xia, J. Liu, J. Wang, X. Fan, S. V. Saviolov, J. Lin and H. J. Fan, *Nat. Commun.*, 2016, **7**, 12122.
63. G. A. Muller, J. B. Cook, H.-S. Kim, S. H. Tolbert and B. Dunn, *Nano Lett.*, 2015, **15**, 1911-1917.
64. V. Augustyn, J. Come, M. A. Lowe, J. W. Kim, P.-L. Taberna, S. H. Tolbert, H. D. Abruña, P. Simon and B. Dunn, *Nat. Mater.*, 2013, **12**, 518.
65. H. Lindström, S. Södergren, A. Solbrand, H. Rensmo, J. Hjelm, A. Hagfeldt and S. E. Lindquist, *J. Phys. Chem. B*, 1997, **101**, 7717-7722.
66. Q. Zhang, M. D. Levi, Q. Dou, Y. Lu, Y. Chai, S. Lei, H. Ji, B. Liu, X. Bu and P. Ma, *Adv. Energy Mater.*, 2018, **9**, 1802707.
67. L. Yang, S. Cheng, J. Wang, X. Ji, Y. Jiang, M. Yao, P. Wu, M. Wang, J. Zhou and M. Liu, *Nano Energy*, 2016, **30**, 293-302.
68. T. H. Wu, D. Hesp, V. Dhanak, C. Collins, F. Braga, L. J. Hardwick and C. C. Hu, *J. Mater. Chem. A*, 2015, **3**, 12786-12795.
69. C. Julien, M. Massot and C. Poinignon, *Spectrochim. Acta A*, 2004, **60**, 689-700.
70. L. Y. Liu, L. J. Su, Y. L. Lu, Q. N. Zhang, L. Zhang, S. L. Lei, S. Q. Shi, M. D. Levi and X. B. Yan, *Adv. Funct. Mater.*, 2019, **29**, 1806778.
71. J. Liu, M. Zheng, X. Shi, H. Zeng and H. Xia, *Adv. Funct. Mater.*, 2016, **26**, 919-930.

72. H. Xia, C. Hong, B. Li, B. Zhao, Z. Lin, M. Zheng, S. V. Savilov and S. M. Aldoshin, *Adv. Funct. Mater.*, 2015, **25**, 627-635.
73. N. Karikalan, C. Karuppiah, S. M. Chen, M. Velmurugan and P. Gnanaprakasam, *Chem.–Eur. J.*, 2017, **23**, 2379-2386.
74. L. Sheng, L. Jiang, T. Wei and Z. Fan, *Small*, 2016, **12**, 5217-5227.
75. E. Lim, C. Jo, M. S. Kim, M. H. Kim, J. Chun, H. Kim, J. Park, K. C. Roh, K. Kang and S. Yoon, *Adv. Funct. Mater.*, 2016, **26**, 3711-3719.
76. P. Y. Tang, L. J. Han, A. Genç, Y. M. He, X. Zhang, L. Zhang, J. R. Galán-Mascarós, J. R. Morante and J. Arbiol, *Nano Energy*, 2016, **22**, 189-201.



## Supplementary Information

### **Achieving a 2.7 V aqueous hybrid supercapacitor by the pH-regulation of electrolyte**

Lijun Su,<sup>a,b</sup> Qingnuan Zhang,<sup>a</sup> Yue Wang,<sup>c</sup> Jianing Meng,<sup>c</sup> Yongtai Xu,<sup>a,b</sup> Lingyang Liu,<sup>a,b</sup> and Xingbin Yan<sup>\*a,b,d</sup>

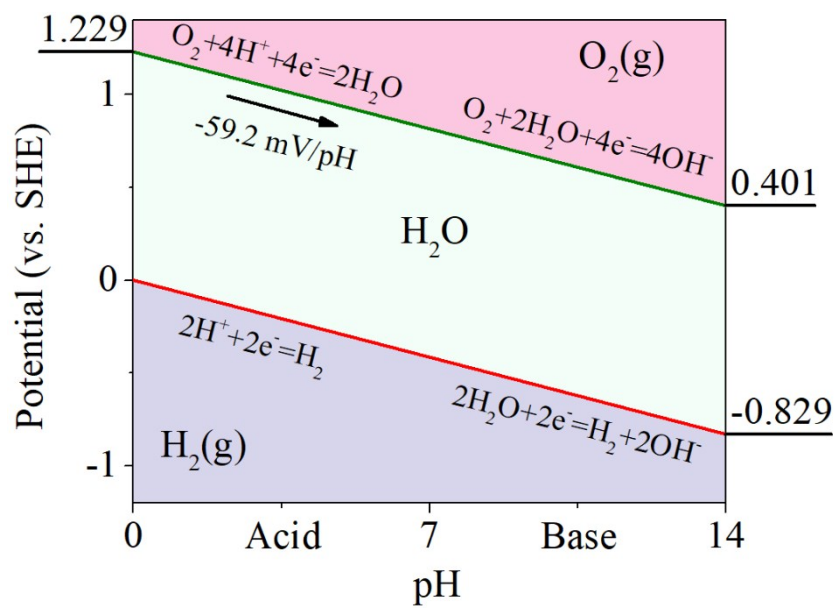
<sup>a</sup> Laboratory of Clean Energy Chemistry and Materials, State Key Laboratory of Solid Lubrication, Lanzhou Institute of Chemical Physics, Chinese Academy of Sciences, Lanzhou 730000, P.R. China.

<sup>b</sup> Center of Materials Science and Optoelectronics Engineering, University of Chinese Academy of Sciences, Beijing 100049, P.R. China.

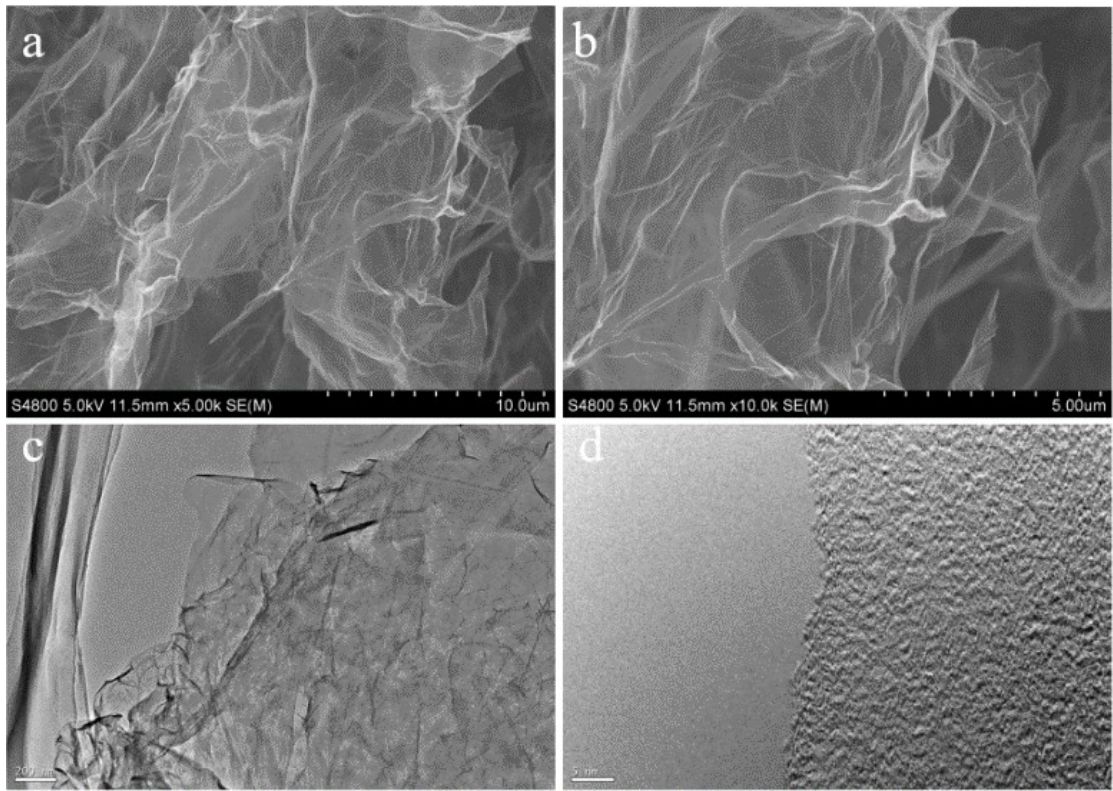
<sup>c</sup> School of Physical Science and Technology, Lanzhou University, Lanzhou, 730000, P.R. China.

<sup>d</sup> Dalian National Laboratory for Clean Energy, Dalian 116023, P.R. China.

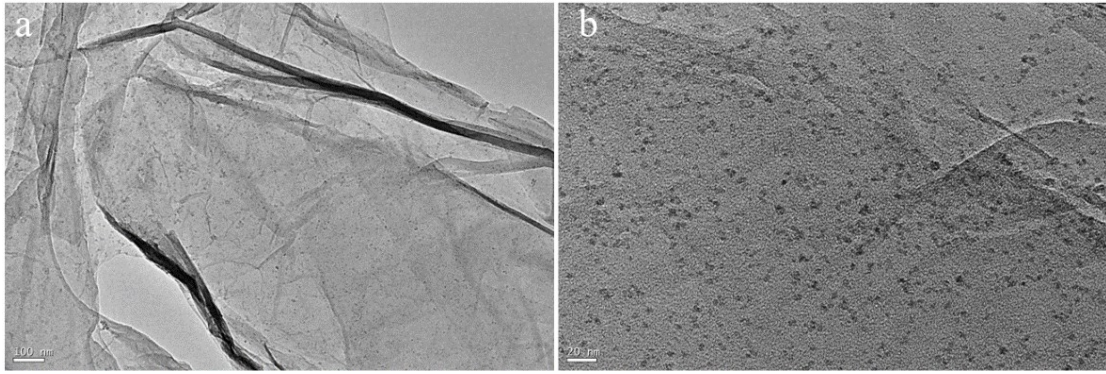
\*Corresponding author: XingBin Yan (email: xbyan@licp.cas.cn)



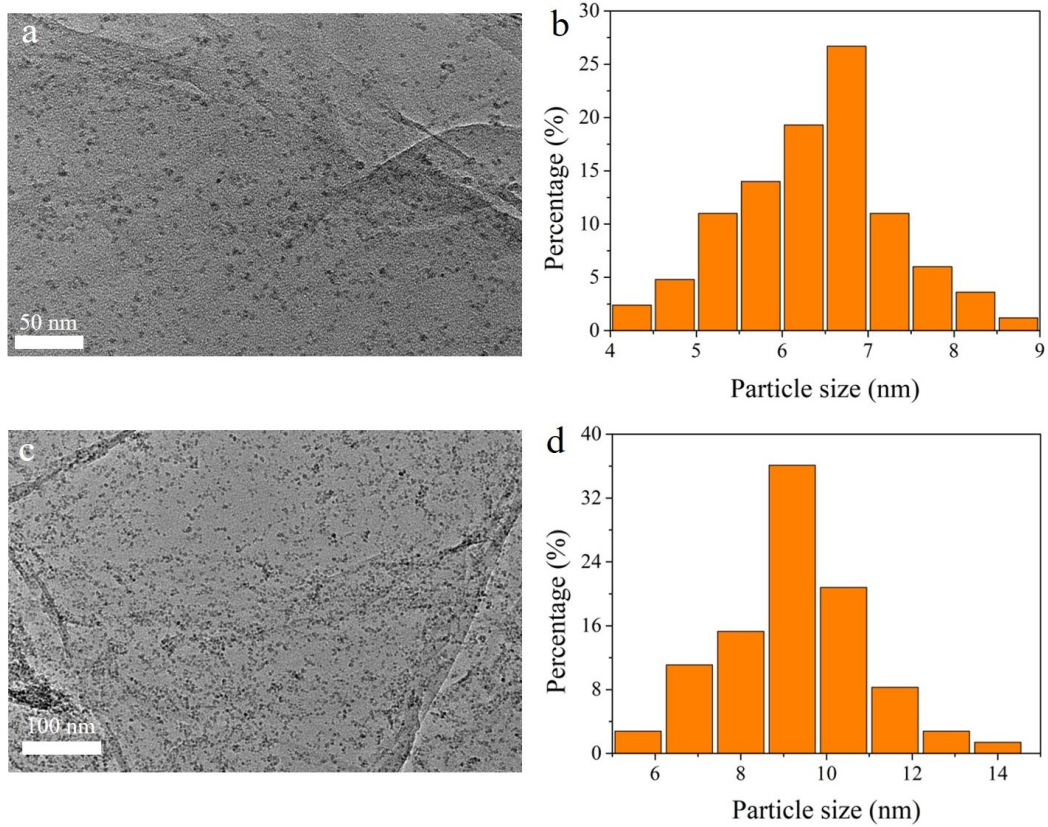
**Figure S1.** Electrochemical stable window of aqueous electrolytes at a constant of 1.23 V as governed by Pourbaix diagram.<sup>1</sup>



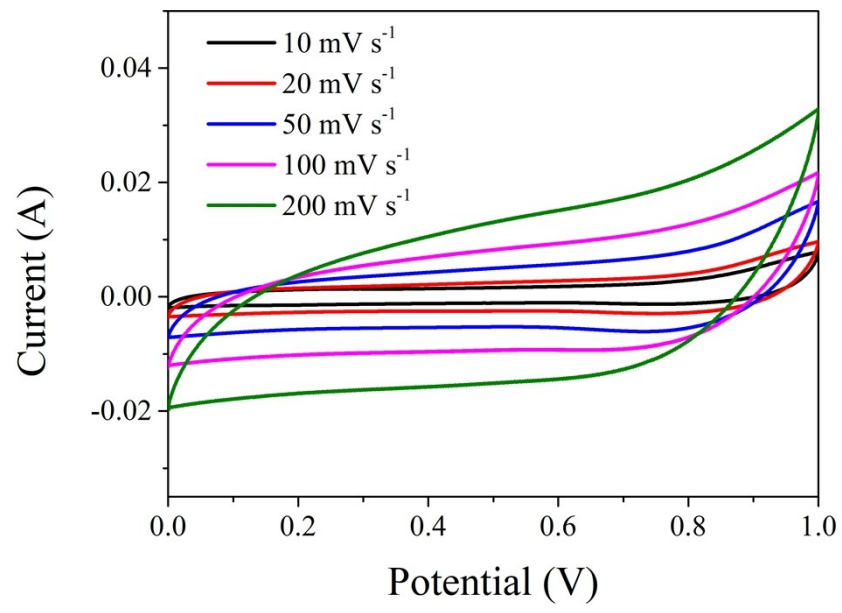
**Figure S2.** SEM images of pure graphene after the first-step solvothermal reaction with scale size of 10  $\mu\text{m}$  (a) and 5  $\mu\text{m}$  (b). TEM images of graphene with scale size of 20 nm (c) and 5 nm (d).



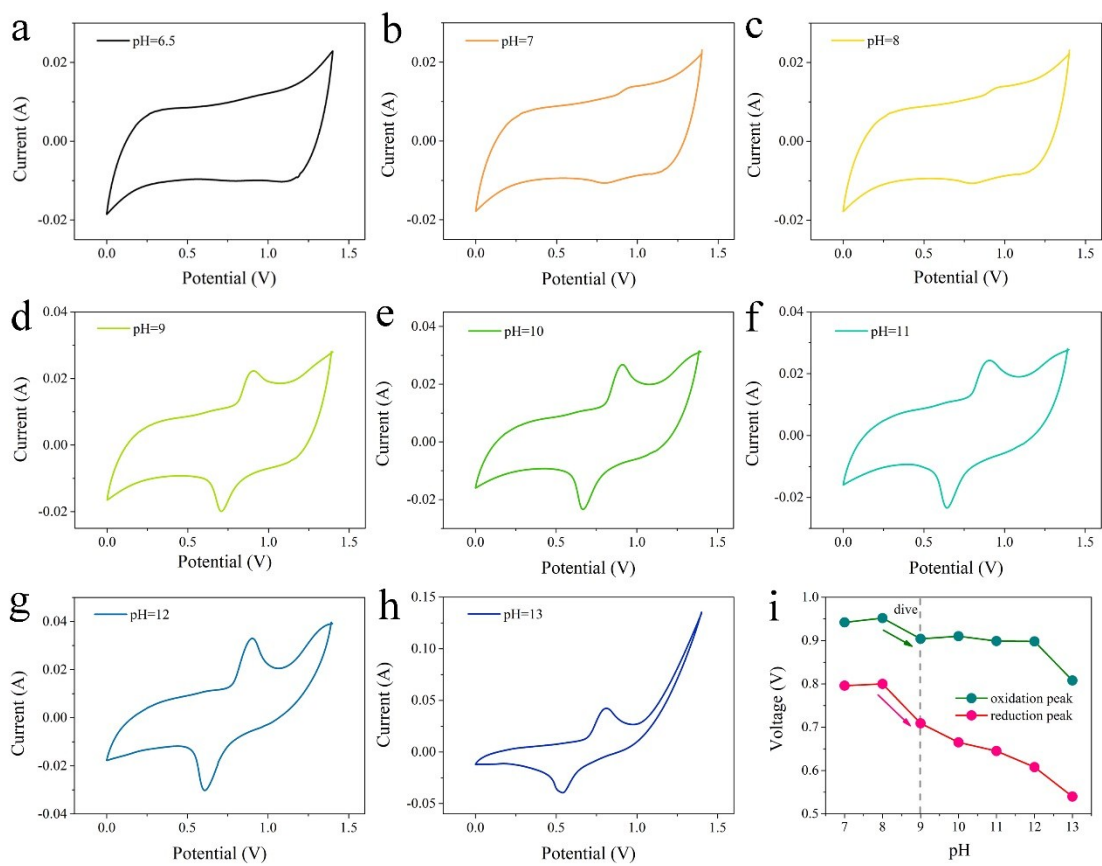
**Figure S3.** TEM images of  $\text{Mn}_3\text{O}_4$  nanodots anchored on graphene with scale size of 100 nm (a) and 20 nm (b).



**Figure S4.** TEM images of Mn<sub>3</sub>O<sub>4</sub>-NDs@NG (a, scale bar is 50 nm) and NMO-NDs@NG (c, scale bar is 100 nm). The statistical size distribution of Mn<sub>3</sub>O<sub>4</sub>-NDs (b) and NMO-NDs (d) by nano measurer software.

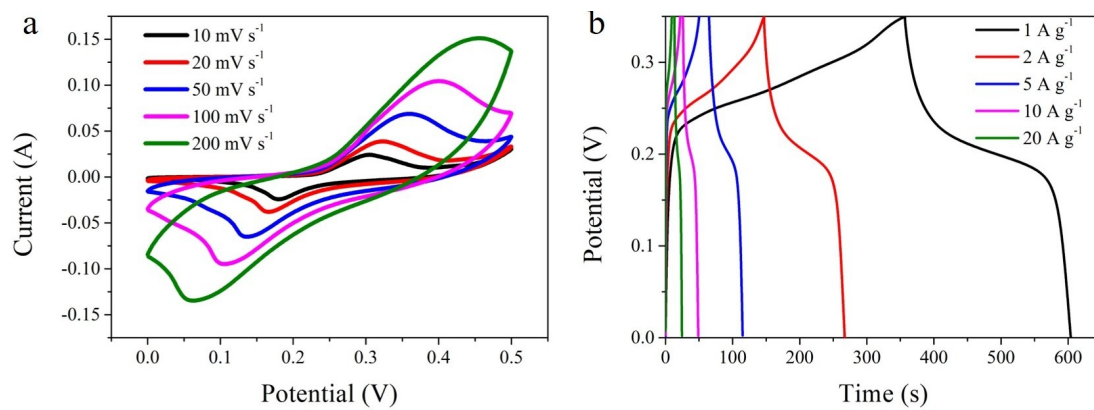


**Figure S5.** The electrochemical performance of NG in Na<sub>2</sub>SO<sub>4</sub> electrolyte. CV curves from 10 to 200 mV s<sup>-1</sup>.



**Figure S6.** (a-h) CV curves of NMO-NDs@NG electrode at the electrolytes with the pH values ranging from 6.5 to 13. (i) The potential position of redox peaks varies with the pH value.

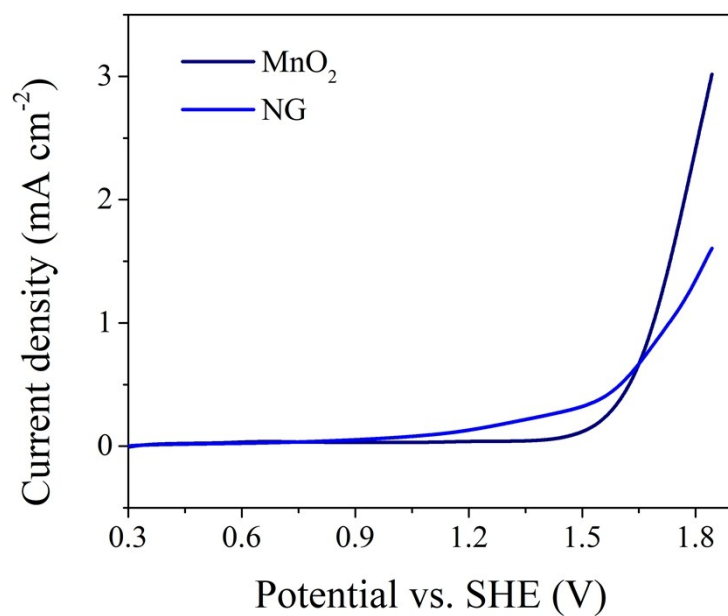




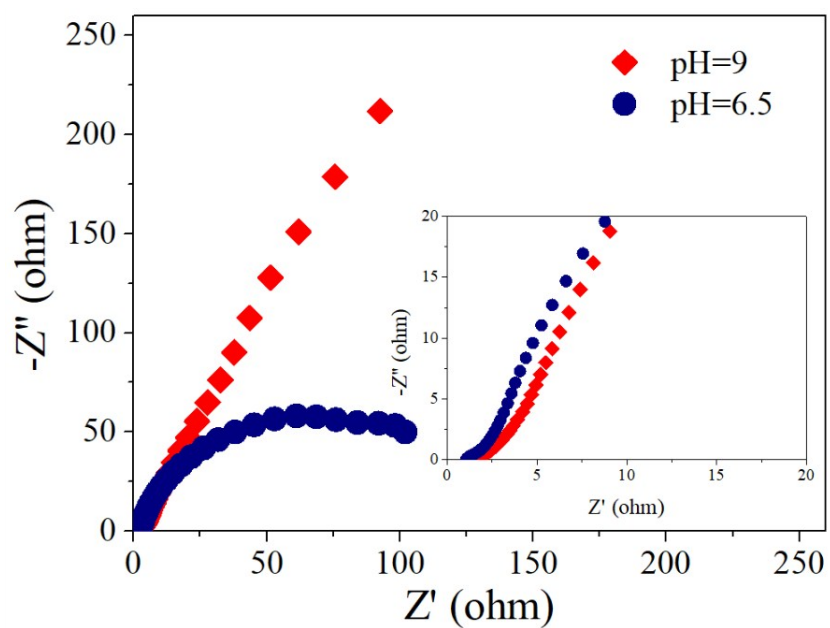
**Figure S7.** The electrochemical performance of NMO-NDs@NG in KOH electrolyte.

(a) CV curves from 10 to 200 mV s<sup>-1</sup>, (b) GCD plots from 1 to 20 A g<sup>-1</sup>.

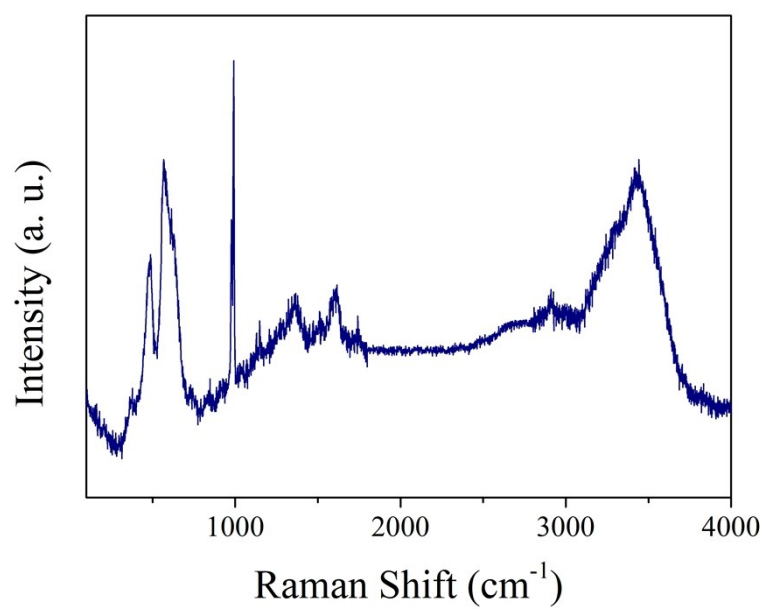




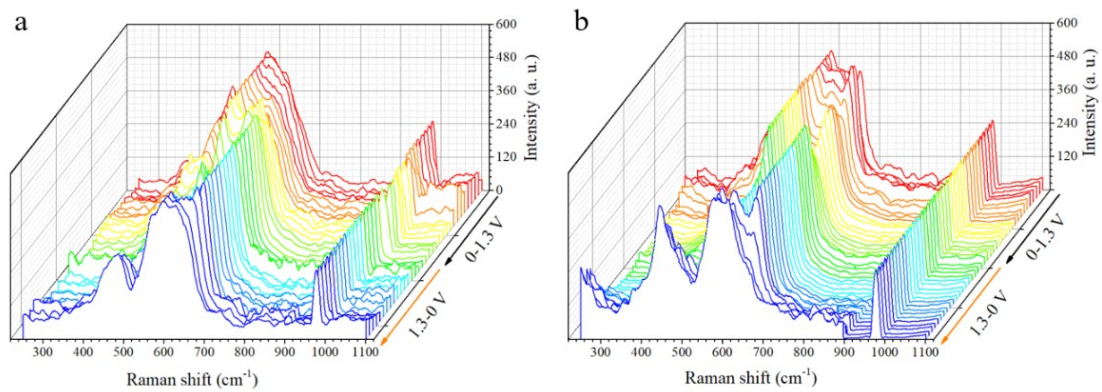
**Figure S8.** Linear sweep voltammetry (LSV) curves of MnO<sub>2</sub> and NG in Na<sub>2</sub>SO<sub>4</sub>-based electrolytes of pH=9 under the three-electrode system and at the scan rate of 10 mV s<sup>-1</sup>.



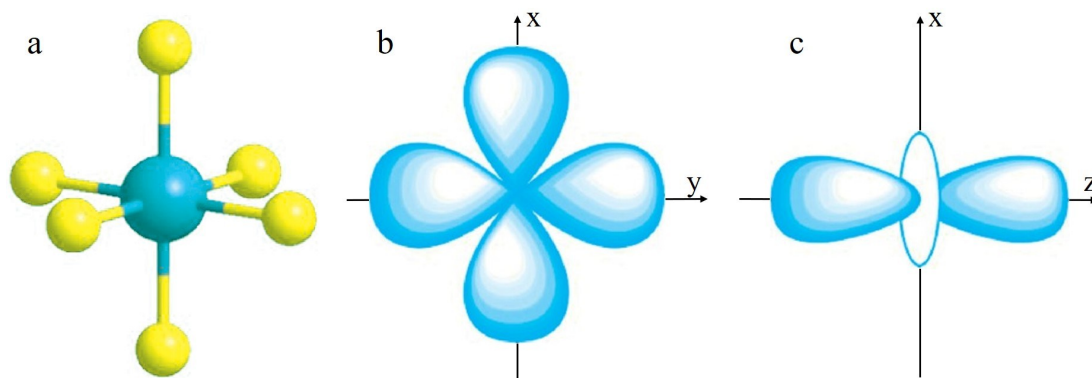
**Figure S9.** The electrochemical impedance spectrum of NMO-NDs@NG at 1.3 V in the electrolytes with pH=6.5 and pH=9. Inset is the enlarged diagram at the high frequency region.



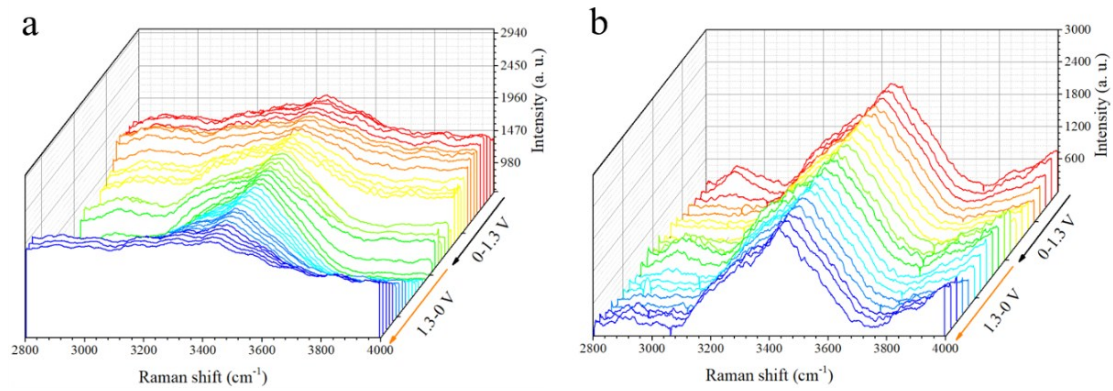
**Figure S10.** Raman spectrum from 100 to 4000 cm<sup>-1</sup> of NMO-NDs@NG in the Na<sub>2</sub>SO<sub>4</sub> electrolyte of pH=9.



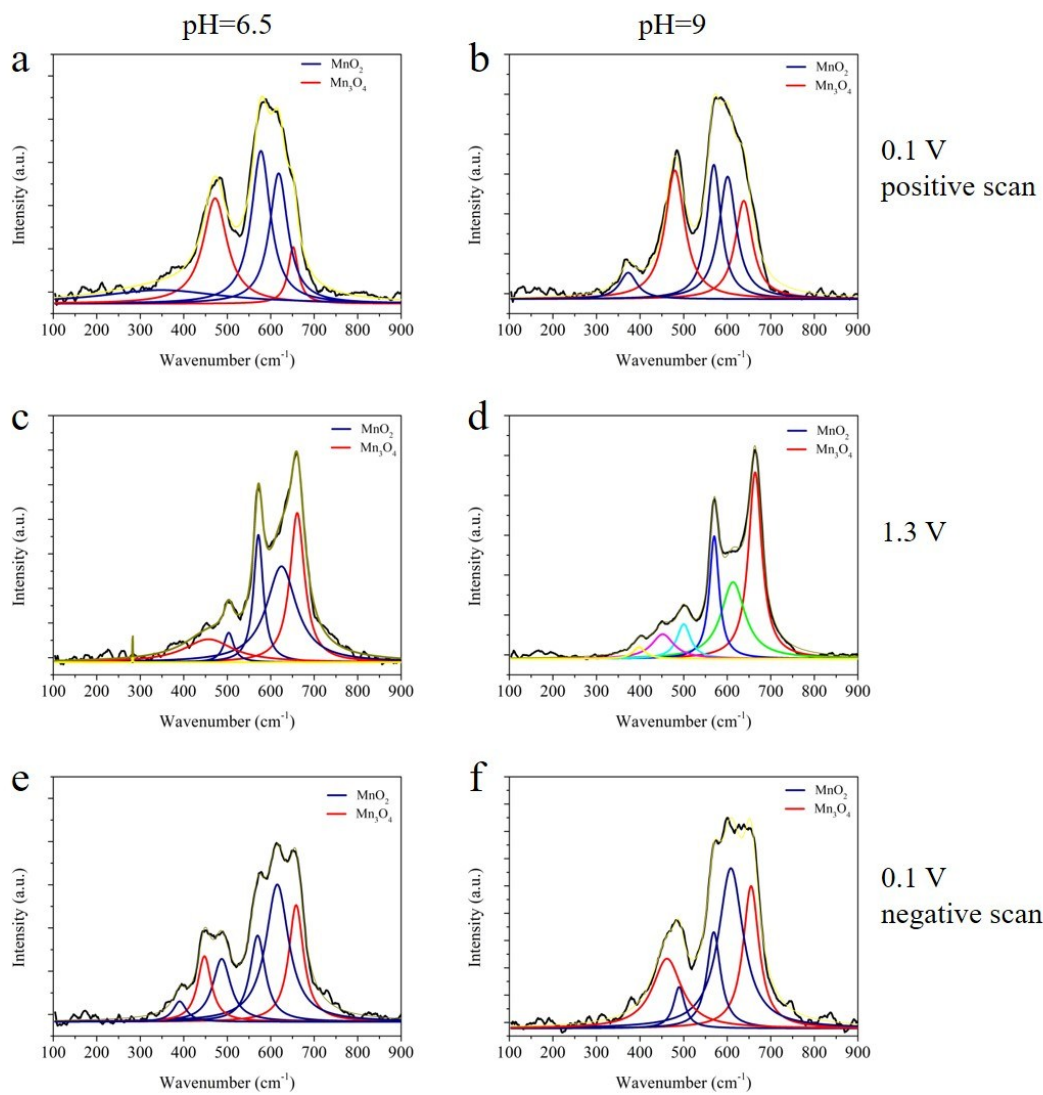
**Figure S11.** Raman spectra of NMO-NDs@NG in the electrolyte of pH=9 (a) and pH=6.5 (b) with the wavenumber from 250 to 1100 cm<sup>-1</sup>.



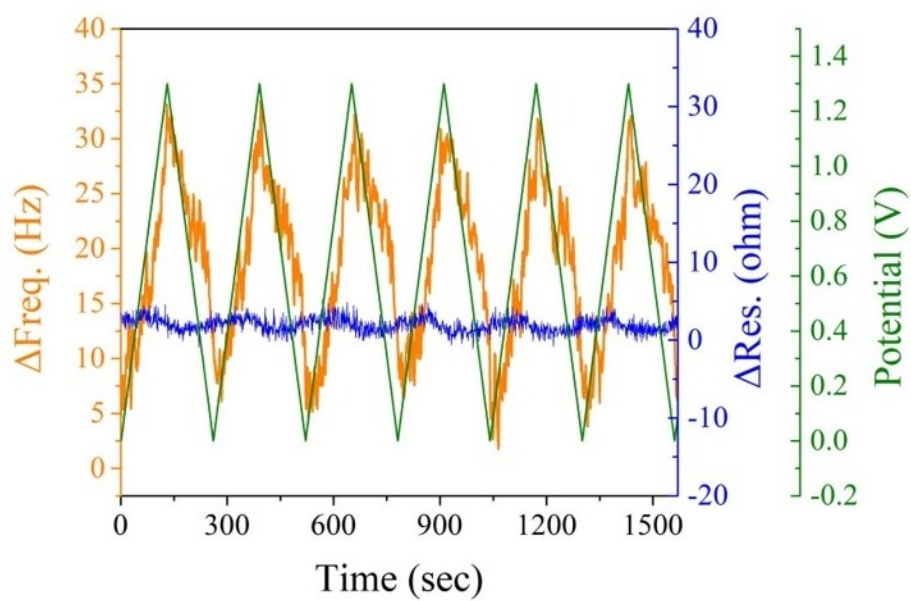
**Figure S12.** The graphical representation of  $[\text{MnO}_6]$  octahedra (a) and the corresponding electron orbitals of  $v_1$  ( $d_z^2$ ) (b) and  $v_2$  ( $d_{x^2-y^2}$ ) (c).<sup>2, 3</sup> Color code: Mn (dark cyan ball); O (yellow ball).



**Figure S13.** The *in-situ* Raman spectrum of the NMO-NDs@NG electrode in the electrolytes of pH=9 (a) and pH=6.5 (b) with the wavenumber from 2800 to 4000  $\text{cm}^{-1}$ .

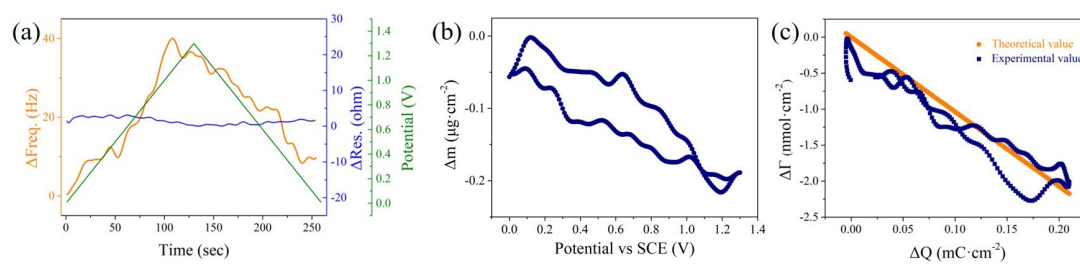


**Figure S14.** Lorentz fitting of in-situ Raman spectrum of NMO-NDs@NG in the electrolytes of pH=6.5 (a, c, e) and in the electrolytes of pH=9 (b, d, f) at the different voltages.

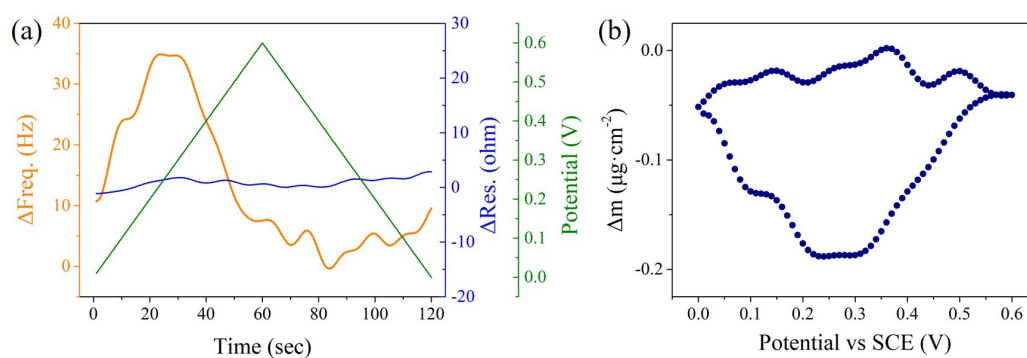


**Figure S15.** Raw EQCM data of NMO-NDs@NG-coated quartz electrodes prepared by VFT technique.

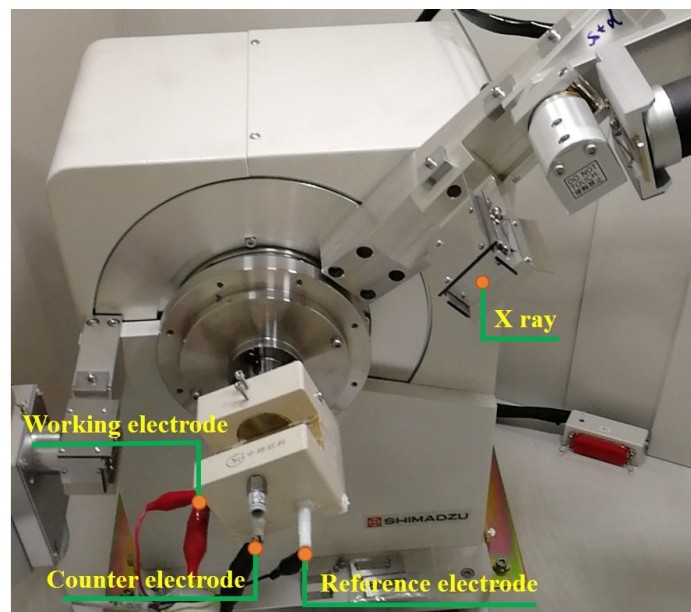




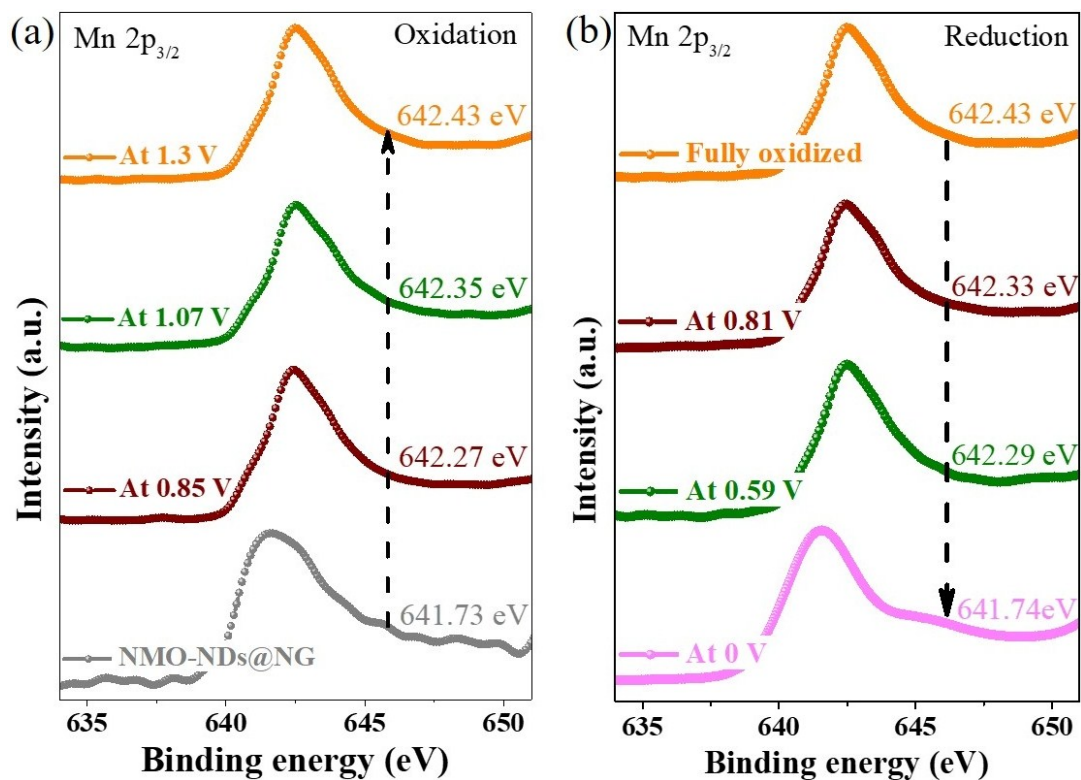
**Figure S16.** EQCM analyze of NMO-NDs@NG in the electrolyte of pH=6.5. (a)  $\Delta Freq.$ ,  $\Delta Res.$  and the potential change as function of time during the charge-discharge cycle. (b)  $\Delta m$  as a function of potential. (c) The theoretical and experimental ion population changes ( $\Delta \Gamma$ ) as a function of  $\Delta Q$  during charging and discharging process for the NMO-NDs@NG electrode.



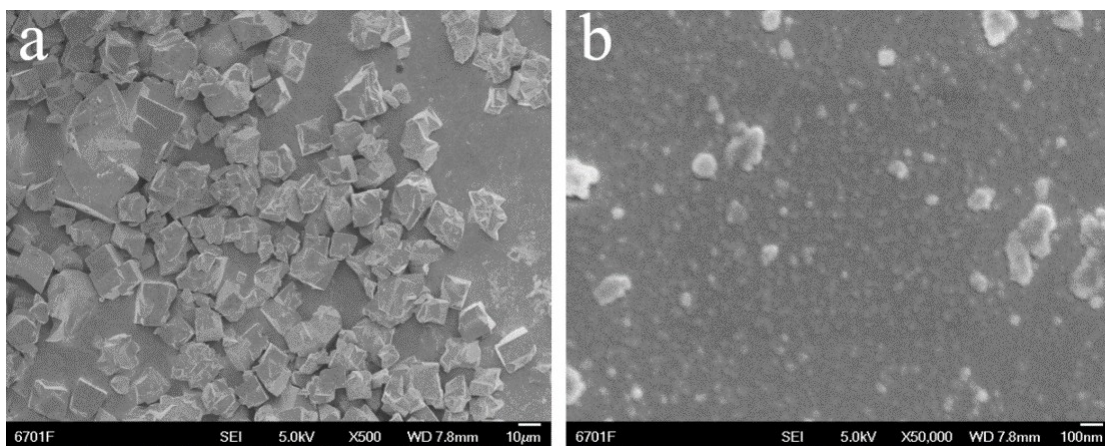
**Figure S17.** EQCM analyze of NMO-NDs@NG in KOH electrolyte. (a)  $\Delta Freq.$ ,  $\Delta Res.$  and the potential change as function of time during the charge-discharge cycle. (b)  $\Delta m$  as a function of potential.



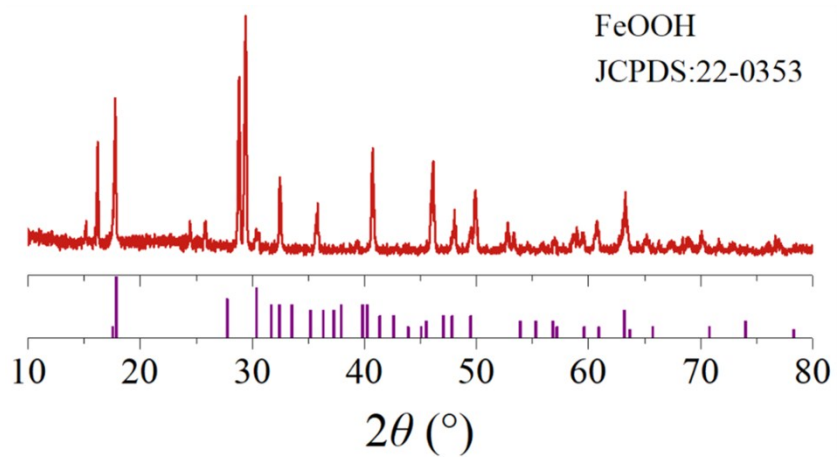
**Figure S18.** The three-electrodes configuration for the in-situ XRD test.



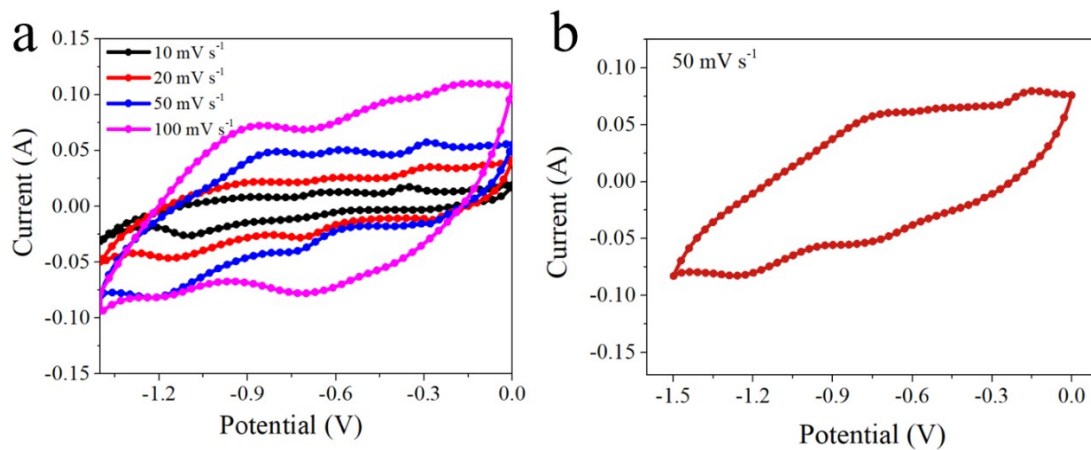
**Figure S19.** Mn 2p<sub>3/2</sub> core-level XPS spectra of the NMO-NDs@NG electrode at different charge (a) and discharge (b) states.



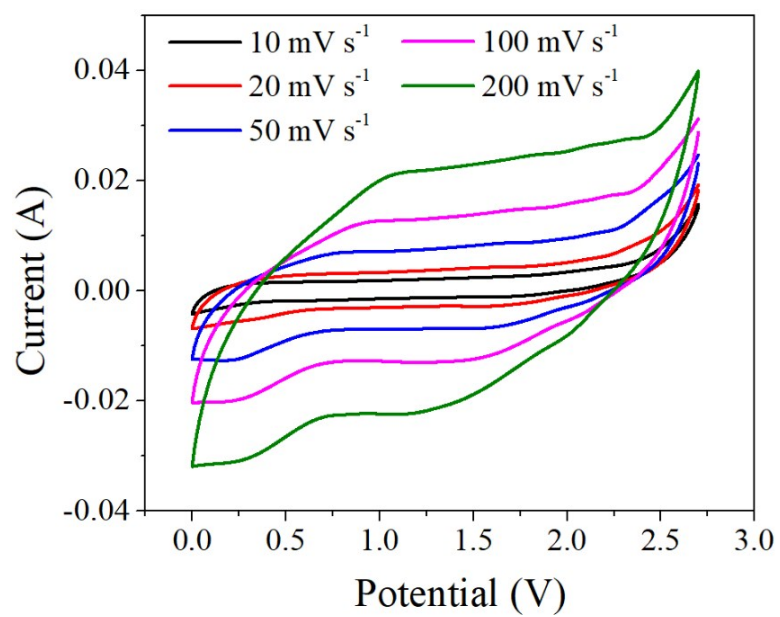
**Figure S20.** SEM images of FeOOH with scale size of 10  $\mu\text{m}$  (a) and 100 nm (b).



**Figure S21.** XRD pattern of FeOOH.



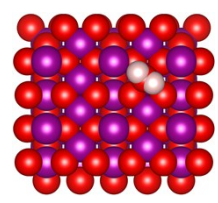
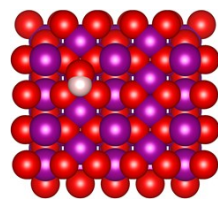
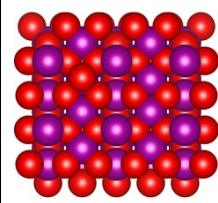
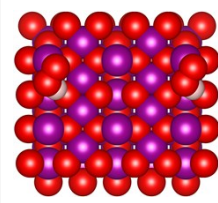
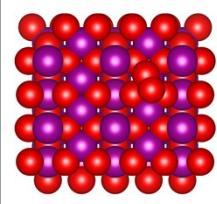
**Figure S22.** CV curves of FeOOH in the electrolyte of pH=9 with a **voltage window** of -1.4-0 V (a) and -1.5-0 V (b).



**Figure S23.** CV curves of NMO-NDs@NG//FeOOH hybrid SC in the neutral Na<sub>2</sub>SO<sub>4</sub> electrolyte (pH=6.5) at scan rates from 10 to 200 mV s<sup>-1</sup>.

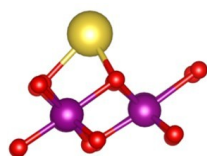
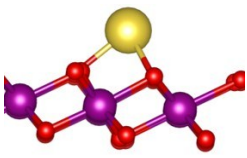
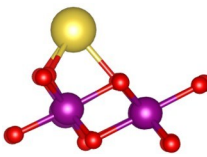
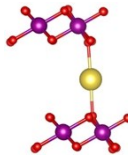
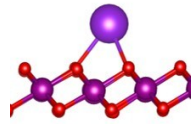
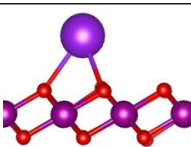
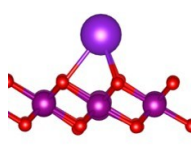
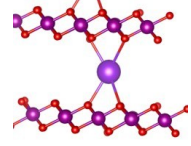
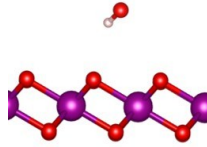


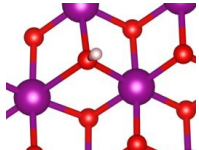
**Table S1.** Free energies at zero potential and the intermediate structures of the OER on O\*-covered NMO(100) surface, obtained by DFT calculations.

				
+2H <sub>2</sub> O(l)	+H <sub>2</sub> O(l)+ <sup>1</sup> / <sub>2</sub> H <sub>2</sub> (g)	+H <sub>2</sub> O(l)+H <sub>2</sub> (g)	+ <sup>3</sup> / <sub>2</sub> H <sub>2</sub> (g)	+O <sub>2</sub> +2H <sub>2</sub> (g)
	ΔE <sub>OH</sub> =0.57 eV	ΔE <sub>O</sub> =2.61 eV	ΔE <sub>HOO</sub> =3.36 eV	
ΔG <sub>water</sub> =0.0 eV	ΔG <sub>OH</sub> =0.92 eV	ΔG <sub>O</sub> =2.66 eV	ΔG <sub>HOO</sub> =3.79 eV	ΔG <sub>O<sub>2</sub></sub> =4.96 eV

Violet spheres represent metal ions, red spheres represent oxygen and white spheres represent hydrogen. DFT binding energies were corrected for zero point energy and change in entropy (at 298 K). The corrections were added to the binding energy and free energies of adsorbed O, OH, and OOH, which were 0.05, 0.35, and 0.40 eV, respectively.

**Table S2.** Spin-polarized DFT calculations: the adsorption energy and the bond length of different adsorption configurations.

Configuration	Adsorption energy ( $E_{\text{ads}}$ , eV)	Bond length (Å)	Atom model
Na-top	-3.32	2.25	
Na-3fh-O	-2.72	2.23	
Na-3fh-Mn	-3.20	2.26	
Na-middle	-3.87	2.46	
K-top	-4.16	2.68	
K-3fh-O	-4.20	2.70	
K-3fh-Mn	-4.17	2.71	
K-middle	-4.45	3.00	
OH-Mn-top	0.11	3.98	

OH-O-vacancy	-3.77	1.99	
--------------	-------	------	---

## Supplementary Note

### Calculation of average crystallite size:

We have calculated the average crystallite size from wide-angle XRD pattern (Figure 1c) for the sample. From the wide-angle XRD pattern, the average crystallite size could be calculated by Debye-Scherrer equation:<sup>4, 5</sup>

$$D = \frac{K\lambda}{\beta \cos \theta}$$

where  $\lambda$  is the X-ray wavelength (0.15405 nm),  $\beta$  is the half height and half width of the diffraction peak (FWHM),  $\theta$  is the diffraction angle,  $K$  is a constant and  $D$  means the average crystallite size. When the FWHM of  $\beta$  is 0.9249,  $\theta$  is 40.66 and  $K$  is 0.9432, the calculated average crystallite size is 9.625 nm.

We have tested the electrochemical performance of NMO-NDs@NG in KOH electrolyte. As shown in Figure S7a, the voltage window of NMO-NDs@NG was 0~0.5 V. And the specific capacity of NMO-NDs@NG was 246 C g<sup>-1</sup> at current density of 1 A g<sup>-1</sup> (Figure S7b). Comparing the energy storage behavior of NMO-NDs@NG in Na<sub>2</sub>SO<sub>4</sub> electrolyte (a surface-controlled pseudocapacitive behavior), NMO-NDs@NG showed a battery-like behavior mainly associated with the reactivity of OH<sup>-</sup> ions in alkaline KOH electrolyte. The results indicated that the charge storage mechanism of NMO-NDs@NG depends largely on the type of electrolytes.

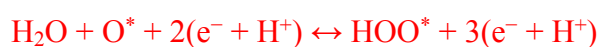
The reactions of water splitting and the corresponding free energies (Figure 4d) can be written as follows:



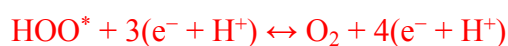
$$\Delta G_1 = \Delta G_{\text{HO}} - \Delta G_{\text{water}}$$



$$\Delta G_2 = \Delta G_{\text{O}} - \Delta G_{\text{HO}}$$



$$\Delta G_3 = \Delta G_{\text{HOO}} - \Delta G_{\text{O}}$$



$$\Delta G_4 = \Delta G_{\text{O}_2} - \Delta G_{\text{HOO}}$$

We have added a full Raman spectrum from 100 to 4000  $\text{cm}^{-1}$  of NMO-NDs@NG in the  $\text{Na}_2\text{SO}_4$  electrolyte of pH=9. As shown in Figure S10, there were three major Raman regions attribute to the Mn-O stretching vibrations of  $[\text{MnO}_6]$  octahedra located at 660-670  $\text{cm}^{-1}$  ( $\nu_1$ ), 569-577  $\text{cm}^{-1}$  ( $\nu_2$ ) and 485-507  $\text{cm}^{-1}$  ( $\nu_3$ ). And the peak located at 980  $\text{cm}^{-1}$  is ascribed to  $\text{SO}_4^{2-}$ . There were two characteristic peaks of D and G peak of NG located at 1300 (D) and 1580 (G)  $\text{cm}^{-1}$ . Because the Raman was tested in aqueous electrolyte of pH=9, there was an obvious O-H stretching vibrations located at 3100-3700  $\text{cm}^{-1}$ .

EQCM measurement can in-situ measure the mass change of an electrode during real-time charging and discharging of the electrode in the presence of difference ions.<sup>6</sup> The

amount of NMO-NDs@NG coated onto the quartz crystal surface is about 40  $\mu\text{g cm}^{-2}$ . The application of EQCM for gravimetric mode implies that the mass change ( $\Delta m$ ) is linked exclusively to the resonant frequency change ( $\Delta Freq.$ ) whereas the simultaneous resonance width change ( $\Delta W$ ) is zero or much smaller than  $\Delta Freq.$ <sup>7, 8</sup> The instrument we used, i.e. Princeton, QCM922A, can measure the resonance resistance change ( $\Delta Res.$ ), which is transformed into the related  $\Delta W$  by the following equation:<sup>9</sup>

$$\Delta W = \frac{16Ae_{26}^2 \rho_q f_q^3}{\pi Z_q^3} \cdot \Delta R$$

where  $e_{26}$  is the piezoelectric stress coefficient ( $9.65 \times 10^{-2} \text{ C m}^{-2}$ ),  $Z_q$  is the acoustic wave impedance ( $8.8 \times 10^6 \text{ kg m}^{-2} \text{ s}^{-1}$ ). Thus, the  $\Delta W$  can be obtained by multiplying the resonance resistance. In our system, the resonance resistance change was about 4  $\Omega$  when the NMO-NDs@NG-coated quartz electrode was cycled between 0 V to 1.3 V (Figure S15). The  $\Delta Freq.$  overwhelmingly prevailed over the  $\Delta W$ , indicating a gravimetric behavior of the quartz-crystal microbalance.

EQCM can measure the  $\Delta Freq.$ , which can be converted to the  $\Delta m$  by Sauerbrey's Equation:<sup>10</sup>

$$\Delta m = - \frac{A \overline{\mu}_q \rho_q}{2f_q^2} \cdot \Delta f = -C_f \cdot \Delta f$$

where  $A$  is the area of active surface ( $0.198 \text{ cm}^2$ ),  $\mu_q$  is the AT-cut quartz constant ( $2.947 \times 10^{11} \text{ g cm}^{-1} \text{ s}^{-2}$ ),  $\rho_q$  is the quartz crystal density ( $2.65 \text{ g cm}^{-3}$ ),  $f_q$  is the reference frequency (9.00 MHz). Here, the sensitivity factor  $C_f$  is  $5.682 \text{ ng Hz}^{-1} \text{ cm}^{-2}$ .

The experimental ion population change ( $\Delta\Gamma$ ) was calculated by the following equation:

$$\Delta\Gamma = \frac{\Delta m}{M_i}$$

where  $\Delta m$  is the mass change,  $M_i$  is the molecular mass, and for  $\Delta Q < 0$ ,  $M_i = M(\text{Na}^+) = 23 \text{ (g mol}^{-1}\text{)}$ .

The theoretical ion population change ( $\Delta\Gamma_{theor}$ ) was calculated by using Faraday's law:

$$\Delta\Gamma_{theor} = \frac{\Delta Q}{nF}$$

where  $\Delta Q$  is the charge passed through the electrode (C),  $n$  is the valence number of the ion ( $n = 1$ ), and  $F$  is the Faraday constant ( $96485 \text{ C mol}^{-1}$ ).

## Supplementary References

1. H. Kim, J. Hong, K. Y. Park, H. Kim, S. W. Kim and K. Kang, *Chem. Rev.*, 2014, **114**, 11788-11827.
2. L. Y. Liu, L. J. Su, Y. L. Lu, Q. N. Zhang, L. Zhang, S. L. Lei, S. Q. Shi, M. D. Levi and X. B. Yan, *Adv. Funct. Mater.*, 2019, **29**, 12.
3. Q. N. Zhang, M. D. Levi, Q. Y. Dou, Y. L. Lu, Y. G. Chai, S. L. Lei, H. X. Ji, B. Liu, X. D. Bu, P. J. Ma and X. B. Yan, *Adv. Energy Mater.*, 2019, **9**, 10.
4. U. Holzwarth and N. Gibson, *Nat. Nanotechnol.*, 2011, **6**, 534-534.
5. P. Thompson, D. E. Cox and J. B. Hastings, *J. Appl. Crystallogr.*, 1987, **20**, 79-83.
6. Q. Zhang, M. D. Levi, Y. Chai, X. Zhang, D. Xiao, Q. Dou, P. Ma, H. Ji and X. Yan, *Small Methods*, 2019, **3**, 1900246.
7. M. D. Levi, S. Sigalov, D. Aurbach and L. Daikhin, *J. Phys. Chem. C*, 2013, **117**, 14876-14889.
8. M. D. Levi, N. Shpigel, S. Sigalov, V. Dargel, L. Daikhin and D. Aurbach, *Electrochim. Acta*, 2017, **232**, 271-284.
9. Johannsmann and Diethelm, *The quartz crystal microbalance in soft matter research*. (Springer, 2015), 10.1007/978-3-319-07836-6, 343-358.
10. M. Hepel, In *Interfacial Electrochemistry: Theory: Experiment, and Applications*, Wieckowski, A., Ed., Marcel Dekker, Inc.: New York, 1999.